Human induced pluripotent stem cell-derived arteries as personalized models of atherosclerosis on-a-chip

Mallone A. [1] *, Gericke C. [2], Hosseini V. [3,4], Vogel V. [3], Chahbi K. [5,6], Walther J. H. [6,7], Haenseler W.[8,9], von Eckardstein A. [10], Emmert M. Y. [1, 12, 13, 14], Weber, B[1,11] §, Hoerstrup, S. P. [1,12] §

1 Laboratory of Tissue Engineering and Disease Modeling, Institute for Regenerative Medicine, University of Zurich, Switzerland

2 Laboratory of Immunology of Neurodegeneration, Institute for Regenerative Medicine, University of Zurich, Switzerland.

3 Laboratory of Applied Mechanobiology, Department of Health Sciences and Technology, ETH Zurich, Switzerland.

4 Center for Minimally Invasive Therapeutics (CMIT), California nanoSystems Institute, UCLA, Los Angeles, USA

5 Department of Mathematics and Computer Science, University of Strasbourg, France

6 Computational Science & Engineering Laboratory, Department of Mathematics, ETH Zurich, Switzerland

7 Laboratory of Fluid Mechanics, Department of Mechanical Engineering, Technical University of Denmark, Denmark

8 Laboratory of Systems and Cell Biology of Neurodegeneration, Institute for Regenerative Medicine, University of Zurich, Switzerland

9 Institute of Molecular Systems Biology, ETH Zurich, Switzerland

10 Institute of Clinical Chemistry, University Hospital Zurich, Switzerland

11 Laboratory of Disease modeling and organoid technology, Department of Dermatology, Medical University of Vienna, Austria

12 Wyss Translational Center Zurich, University of Zurich and ETH Zurich, Zurich, Switzerland

13 Department of Cardiothoracic and Vascular Surgery, German Heart Center Berlin, Berlin, Germany

14 Department of Cardiovascular Surgery, Charité Universitätsmedizin Berlin, Berlin, Germany

§ These authors jointly supervised the work

* Correspondence to
anna.mallone@irem.uzh.ch, simon. hoerstrup@irem.uzh.ch

Abstract

Atherosclerosis is a disease of the cardiovascular system characterized by local chronic inflammation. The disease's hallmarks are vessel stenosis, stiffening, and hyperplasia, which are the most prominent underlying causes of cardiovascular complications. Cells from the innate immune response have a central role in disease development as they orchestrate inflammatory events leading to the deposition of fatty streaks in the sub-endothelium. The negative remodeling of atherosclerotic vessels is exacerbated by local variations of intraluminal hemodynamic load, where disturbed blood flow aggravates plaque deposition. Despite pioneering efforts to explore the relationship between inflammation and hemodynamics in the disease framework, interactions between these two elements have never been investigated *in vitro* before due to the lack of modeling systems with an adequate degree of complexity. Here, we employed a multifaced approach combining computational fluid dynamics (CFD) and tissue-engineering to achieve, for the first time *in vitro*, the full development of human atherosclerotic plaques within a one-month timeframe. We established the atherosclerosis-on-a-chip model using human induced pluripotent stem cells-derived populations assembled into tissue-engineered arterial vessels and cultured in atheroprone conditions. We reliably predicted regions of plaque deposition within the vessels via tailored CFD modeling. Using machine-learning-aided immunophenotyping and molecular analyses, we found that immune cell populations and extracellular matrix (ECM) components from modeled plaques were comparable to those in human carotid lesions. Furthermore, we discovered similarities between the ECM tensional state of tissue-engineered and native plaques by performing nanoprobe-based tensile analyses. Our results provide the *in vitro* proof of the link between hemodynamics and inflammation in atherosclerosis and present a personalized, up-scalable tool to study human arterial atherosclerosis onset and progression. We anticipate our work to represent a milestone in the atherosclerosis modeling and precision medicine arena and to serve as a starting point for in-depth analyses targeted at more specific disease progression stages.

Introduction

Atherosclerosis is an inflammatory disease affecting the arterial walls and is associated with life-threatening events such as myocardial infarction or stroke [1,2,3]. The hallmarks of the disease are intra-vessel fibrotic and fatty aggregates causing abnormal vascular narrowing and leading to diverse outcomes depending on the downstream affected organ or vasculature[4]. Besides those cases of ascertained genetic predisposition (i.e., familial hypercholesterolemia), multivariate factors can contribute to the development of sporadic atherosclerosis. Among those, dyslipidemia with high blood levels of low-density lipoproteins (LDL), and chronic inflammation have been correlated with the disease's extent together with age- and lifestyle-related comorbidities as smoking, diabetes and hypertension[5-8]. Some of these factors reflect systemic changes in blood hemodynamics that cause major alterations in flow patterns (e.g., vortexes and turbulences), exerting novel stresses on the vessel walls. Ultimately, these flow variations affect the integrity of the endothelial layer, promoting the local sub-luminal accumulation of LDL, and providing the initial trigger for an inflammatory response[9,10]. Although 2D *in vitro* models based on adherent cell cultures revealed the underlying mechanisms of endothelial and immune cell activation upon local variations in lipoproteins concentrations[11-14], and mouse models provided insights on ECM remodeling by inflammatory cells[15], the behavior of these cells in regions of hemodynamic perturbation and in a human native-like 3D vascular environment, including their effect on vascular extracellular matrix remodeling, remains largely unknown.

While some 3D tissue-engineered models (i.e. microtissues and organoids) have attempted to mimic the early and late stages of the disease [16,17], to the best of our knowledge, to date, none of them was able to replicate the complex process of plaque buildup in a tissue-engineered replica of a human artery. It is proven that regions in the vessel lumen exposed to a disturbed blood flow correlate with the location of atherosclerotic streaks[18] and that local vascular inflammation is triggered by activated endothelial cells and sub-endothelial lipoproteins stagnation led by disturbed hemodynamics[11,19]. Based on this evidence, we hypothesized whether it is possible to anticipate the exact location of lipoproteins accumulation in the vessels by adopting a computational fluid dynamic (CFD) approach, thus predicting potential plaque deposition areas in a biological system. Next, by introducing physio-pathological levels

of circulating inflammatory cells and hyperlipidemic levels of LDL, we further hypothesized whether it is possible to accelerate plaque formation *in vitro*, a process that usually takes decades in humans[20]. To test our hypotheses, first, we developed an *in silico* model that included LDL-like particles in a dynamic pulsatile environment. The model allowed us to predict potential intimal hyperplasia regions and measure the potential sub-endothelial accumulation of LDL particles. To validate our predictions, we replicated such an environment *in vitro* by setting up a fluidic device hosting multiple 3D tissue-engineered small-caliber vascular grafts connected to a bioreactor system. We exploited protocols previously developed, now used for tissue-engineered valvular and vascular constructs in preclinical phases, based on the use of biodegradable polyglycolic-poly4-hydroxybutyrate (PGA-P4HB) scaffolds[21-25].We adapted such protocols to engineer autologous small-caliber vessels that we generated from human induced pluripotent stem cell (iPSC) – derived endothelial and smooth muscle cells. After 4 weeks of culture, we obtained native like small caliber vessels which were then used to to model atherosclerotic disease by introducing different atheroprone features (hyperlipidemia, inflammation, and disturbed hemodynamics) for a total period of 28 days.

We observed the formation of hyperplastic regions where CFD-predicted flow displayed pathophysiological flow pattern with a drop in velocity and wall shear stress and increased flow disturbances characterized by vortices and whirlpools. These regions were flanked by hot-spots of high intraluminal pressure. Hence, we investigated the cellular content of the hyperplastic regions with multiparameter flow cytometry combined with machine-learning-guided t-stochastic neighbor embedding analysis, and we found cell populations comparable with native carotid plaques and in line with previous findings[17,26]. Since intravascular luminal areas of disturbed blood flow have been associated with alteration of elastin and collagens in atherosclerotic lesions[27-29], we investigated the extracellular matrix (ECM) content of the modeled plaques and compared it to native plaques, uncovering similarities in collagen I, II, III, elastin, and other ECM-remodeling proteins at the transcriptional level. Finally, based on the evidence that disturbed hemodynamics in atherosclerotic regions enhances fibronectin (Fn) expression[30], locally affecting ECM crosslinking and increasing vascular stiffness[31,32], we used our model to assess the mechanical strain of fibronectin (Fn) fibers within the modeled plaques. To assess this, we employed a mechanosensitive nanoprobe, the bacterial

fibronectin-binding peptide 5 (Fn-BPA5)[33], demonstrating a targeted binding to the plaque region that was confirmed in native plaque specimens. Our atherosclerosis-on-a-chip model presented in this work pioneers multiplexing approaches in vascular tissue engineering and foster investigative approaches to reveal patient-dependent disease outcomes, patients' susceptibility to new drugs, and even the feasibility of new biocompatible diagnostic tools to both identify vessel regions affected by atherosclerotic plaques, and to assess treatment effectiveness.

Results

1. iPSCs-derived 3D human vessels display tissue architecture comparable to human native vasculature.

To develop fully autologous vessels, we first differentiated iPSCs towards arterial endothelial cells (iECs) (FIGURE 1 a-d, Supplementary figure 1). iECs grew in a confluent monolayer with cobblestone morphology, similar to what is observed for other cell lines used in vascular tissue engineering (VTE) such as human umbilical vein endothelial cells (HUVECs) or human brain microvascular endothelial cells (HBMECs)[34](FIGURE 1a). We characterized the iECs using flow-cytometry. We analyzed the flow data using machine-learning-guided analysis and displayed the multidimensional data in two-dimensional t-SNE plots (FIGURE 1b). We observed that iECs are mainly constituted by CD31+/CD144+/CD68+^{high} cells (cluster 1, 92.45 %), also identified in HUVECs and HMBECs (FIGURE 1b, Supplementary figure 1b). We found other satellite cell clusters displaying high levels of CD31 and CD144 and lower surface levels of scavenger receptor CD68 (cluster 10, 0.05%; cluster 6, 0.35%; cluster 8, 1.4%). iECs phenotype was further confirmed via immunofluorescence staining (IF) showing surface expression of CD31 and vascular endothelial cadherin (VE-Cadh alias CD144) (Supplementary figure 1c, d). Some iECs reached full maturation displaying presence of intracellular von Willebrand factor (vWF) and endothelial nitric oxide synthase (eNOS) (FIGURE 1c). With the investigation of the iECs gene expression profile we additionally confirmed the endothelial phenotype post-differentiation (Supplementary figure 1e). iECs significantly downregulated pluripotency genes *SOX2* ($p < 0.001$), *NANOG* ($p < 0.001$) and *OCT4* ($p < 0.001$), and showed no significant differences in expression levels of the key endothelial genes *VE-CADH* and *CD31* when compared to HUVECs (*VE-CADH* $p = 0.45$, *CD31* $p = 0.09$) and HBMECs (*VE-CADH* $p = 0.39$, *CD31* $p = 0.07$). To test iECs functionality, we performed a tube formation assay, where we showed that iECs have the ability to sprout and generate new cell-to-cell contacts and micro-vascular networks as for HUVECs and HBMECs (FIGURE 1d).

Second, we differentiated contractile smooth muscle cells (iSMCs) from iPSCs, syngeneic to their endothelial cell counterparts (FIGURE 1 e-k, Supplementary figure 2a). In IF experiments, iSMCs displayed typical smooth muscle markers such as smooth muscle myosin heavy chain (SMMHC),

smooth muscle protein 22a (SM22a) and smooth muscle actin alpha (aSMA) (FIGURE 1 f,g). After 5 passages of maturation in metabolic medium, we observed and increase of intracellular aSMA levels, supporting our choice of post-differentiation cell-selection strategy (Supplementary figure 2b, c). We also confirmed the SMCs phenotype by RT-qPCR, where we observed downregulation of pluripotency genes *SOX2* ($p < 0.001$), *OCT4* ($p < 0.001$) and *NANOG* ($p < 0.001$) and upregulation of the signature smooth muscle genes *aSMA* ($p = 0.03$) and *SMTN* ($p = 0.03$) (FIGURE 1e). We investigated iSMCs functionality upon differentiation using both a hydrogel contraction and a wound healing assay. We confirmed the phenotype of iSMCs, showing a contractile behavior comparable to human umbilical vein myofibroblasts (HUVMs vs iSMCs ns: $p > 0.05$). Indeed, HUVMs and SMCs had similar contracting phenotype when compared to the non-contractile human aortic fibroblasts (HUVMs vs HAFs $p = 0.02$, iSMCs vs HAFs $0.02 < p < 0.03$) (FIGURE 1h, i). The wound healing assay proved the ability of iSMCs to convert to a disease-associated synthetic state upon serum starvation[35], and to acquire migration skills. Here, upon starvation, iSMCs showed again a similar behavior to HUVMs (iSMCs vs HUVMs ns $p > 0.05$) but significantly different from HAFs (HUVMs vs HAFs $p = 0.02$, iSMCs vs HAFs $0.008 < p < 0.001$) (FIGURE 1 i,j).

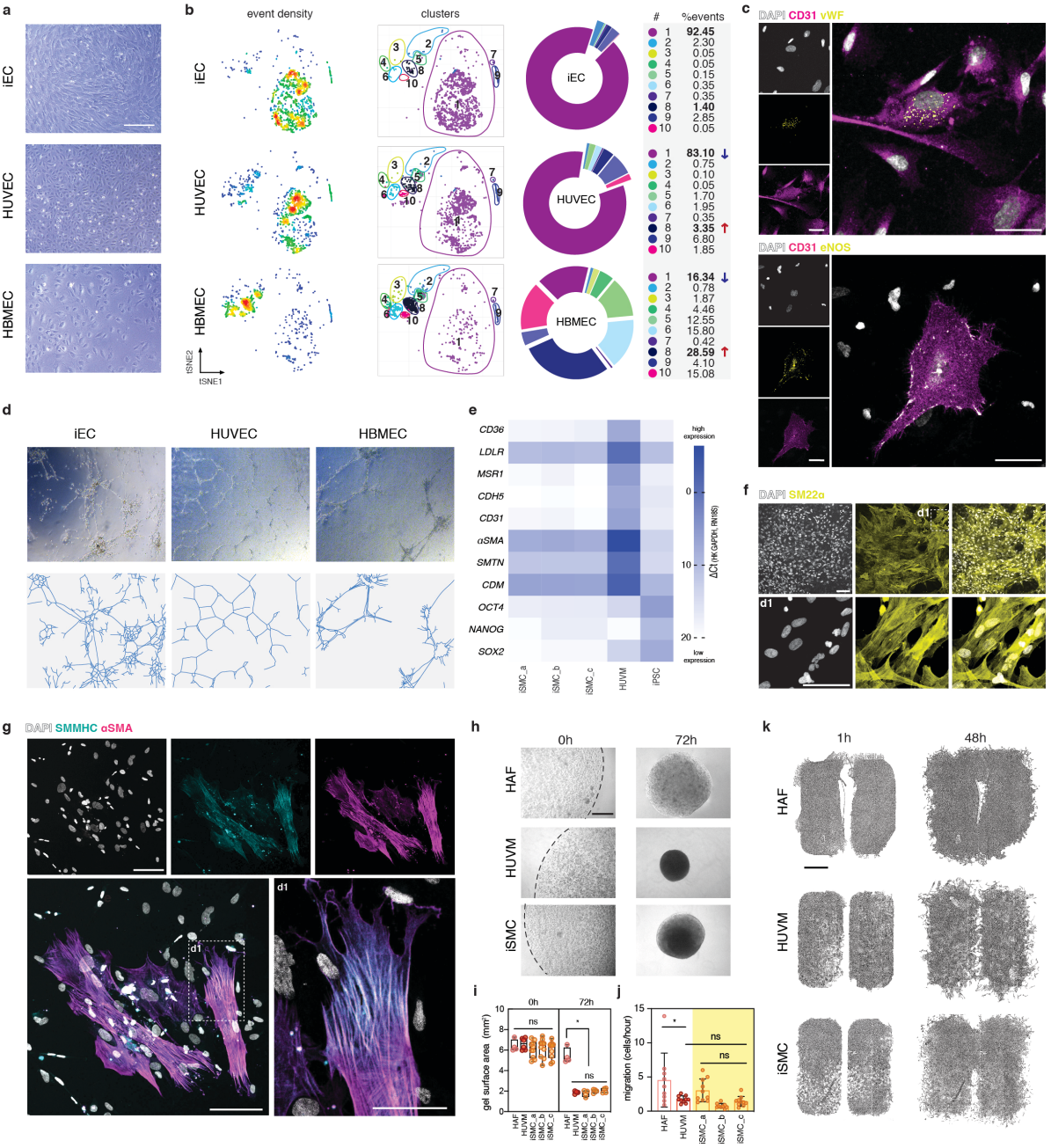

Figure 1. Generation and characterization of syngeneic endothelial and smooth muscle cells from iPSCs for vascular tissue engineering. (a) Bright field images of iECs, HUVECs and HBMECs. Scale bar 250µm. (b) Flow cytometry characterization of different endothelial cells (iECs, HUVECs, and HBMECs) with a multicolor and poli-marker panel. Multidimensional data are showed in 2D t-SNE plots. Event density, FlowSOM clusters and cluster abundances (% of events) are shown. Red arrows indicate cell clusters with increased abundance in HUVECs and HBMECs (vs iECs), and blue arrows indicate cell clusters with decreased abundance in HUVECs and HBMECs (vs iECs). (c) IF characterization of iECs. iECs express CD31, vWF, and eNOS. Scale bars 50µm. (d) Characterization of iECs functionality via tube formation assay. (e) Characterization of iSMC differentiation through RT-qPCR. HUVMs and iPSCs are used as positive and negative controls respectively. (f) iSMCs expression of the smooth muscle protein SM22a. d1= detail. Scale bars 100µm. (g) iSMCs expression of SMMHC and aSMA. d1= detail. Scale bars 100µm. (h-i) Characterization of iSMCs functionality using a fibrin gel contraction assay. Assay duration = 72h. Scale bar 250µm. (j-k) Characterization of iSMCs plasticity with wound healing assay. Assay duration = 48h, Scale bar 2mm. *p* values are reported in the text.

To generate small-caliber vessels mimicking the arterial anatomy, we developed an up-scalable tissue-engineering (TE) approach. We fabricated a microfluidic device suitable for connection with a mechanic pulsatile flow system, promoting tissue culturing in a dynamic, native-like environment (FIGURE 2a-e, Supplementary figure 3, Supplementary video 1, Supplementary CAD files 1-5). For the fluidic chamber, we used a combination of poly-methyl methacrylate (PMMA), aluminum and silicon (VMQ), which were excised from raw material using Computerized Numerical Control (CNC)-based technologies (Supplementary figure 3a, b). We performed a computational fluid dynamic analysis of the respective fluid domain considering a perfusion through the inlet pipe at the constant flow rate of 10 ml/min (velocity of 0.024 m/s) and a density of 999kg/m^3, with a dynamic viscosity of 7.8E-4 Pa-s (Supplementary figure 3c-e). We obtained a stable steady-state solution, characterized by a low Reynolds number of 64, indicating the presence of laminar flow within the device. The CFD predicted arteriolar-like flow velocity, ranging between 0.03 and 0.15 m/s, at the vessel inlet/outlet and at the lumen, respectively (Figure 2d, Supplementary figure 4). The total culturing pressure predicted by the model was ranging from 127 Pa (1 mmHg) at the inlets, to about 20 Pa (0.1 mmHg) at the outlets (Figure 2c). Importantly, the results were comparable at each outlet of the microfluidic device independently from the conduit position, thus confirming the suitability of the device to multiplexing and high-reproducibility approaches (Fligure 2c-d, Supplementary figure 3e, Supplementary CAD file 6, Supplementary simulation file 1). To verify the reliability of our model, we resolved a second case, with a set velocity at the inlet of 0.1 m/s. We observed the formation of steady vortices and whirlpools at the inlet of each vessel in both the 0.1 m/s and the 0.024 m/s cases. Such flow variations, colocalized at the inlet with regions of low shear stress positioned ahead of flow bifurcations and were absent at the outlets (Figure 2e, Supplementary figure 5).

We then combined allogenic iECs and iSMCs into tissue-engineered arteries. First, we seeded iSMCs onto fully biodegradable PGA/P4HB tubular-shaped conduits. We used a fibrin hydrogel carrier to maximize cell retention in the scaffold mesh, and we cultured the seeded constructs through cyclic static and dynamic stimuli for a total of 2 weeks. Second, we coated the inner lumen of the conduits with iECs followed by 2 additional weeks of culture, for a total tissue-engineering period of 1 month (Figure 2f-h). We compared the tissue bioengineered vessels to healthy, native, umbilical veins and to

diseased carotid arteries from human specimens. The artificial vessels showed lumen endothelialization concomitant with collagen IV accumulation throughout the para-luminal area, and with the formation of confined, multicellular media layers perpendicularly aligned to the flow direction. The engineered media layers were overall thicker than those of native umbilical veins and consistently thinner than the media layer of hyperplastic carotid arteries (Figure 2h). Taken together, these observations suggest that our *in vitro* dynamic culturing setup as well as the tissue-engineering strategy employed in this study, promote the assembly of a sub-endothelial basal lamina and foster the formation of a stratified, native-like arteriolar microanatomy.

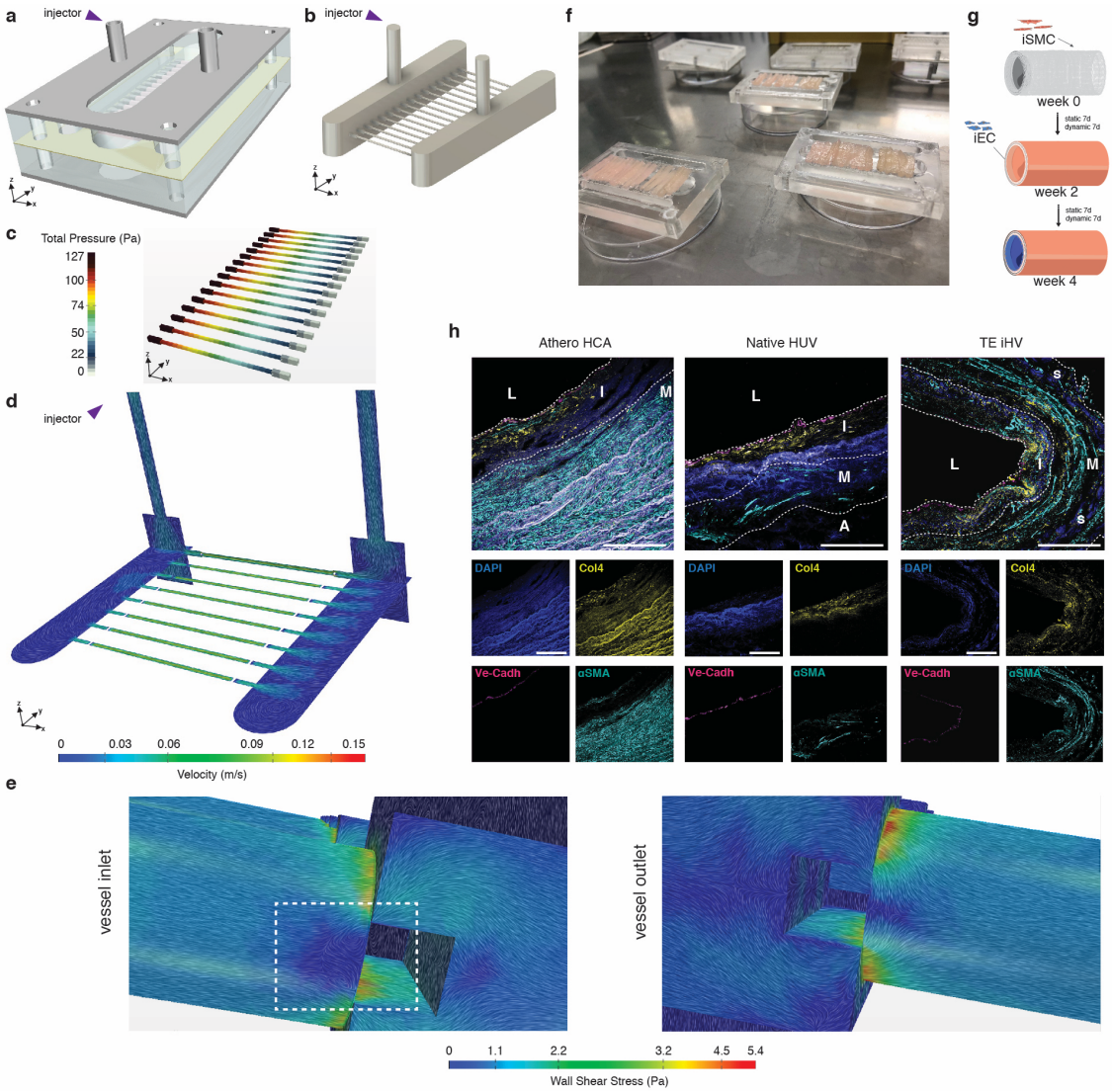

Figure 2. Small-caliber iPSC-derived tissue engineered arteries. (a) CAD model of the assembled fluidic chamber. (b) Flow domain. Inner volume of the chamber occupied by culturing medium. (c) Depiction of the pressure gradient within the tissue-engineered vessels. (d) Cross-sectional and longitudinal view of the flow velocity in the chamber and in the tissue-engineered vessels. (e) Wall shear stress at the inlet and outlet of the vessels. The velocity field is superimposed and depicted using the line integral convolution. Whirlpools are highlighted in the rectangle. (f) Multiple sterile fluidic chambers loaded with tissue-engineered vessels after intraluminal seeding of iECs. (g) Schematics of the adapted tissue-engineering strategy adopted in the study. (h) Immunohistochemistry comparison of carotid arteries form patients' samples (Athero HCA), Native human umbilical veins (Native HUV), and tissue-engineered arteries from iPSCs (TE iHV). L = lumen, I = intima layer, M = media layer, S = scaffold remains. Scale bars 100µm.

2. Computational fluid-dynamic analysis predicts atheroprone, hyperplasic, LDL-laden inflammatory niches in tissue-engineered small-caliber arteries cultured *in vitro*.

We adapted the model by introducing LDL particles at the inlet boundary as a concertation field (passive scalar). We modeled advection, drag, lift forces and random motion caused by the diffusion of the particles in the fluid domain, using a diffusion constant representing the diffusion of the LDL particle. The mass flow inlet generated a flux of LDL particles into the inlet pipe, and subsequently produced downstream fluxes on the surfaces of the vessels (Figure 3b, g). We assumed that LDL particles touching the vessel walls would adhere to the surface and not influence or block any subsequent impact of other particles. In We measured that about 1.8% of the overall LDL perfused at the inlet remained within device after each iteration. In our calculations, we assumed 9 medium changes (one every 3 days of culture), and that at every 100 bioreactor cycles (about the time for the medium to recirculate the bioreactor system) the LDL concentration at the inlet would be 180% reduced from the preceding value. We elaborated a dynamic surface growth prediction where we calculated a putative degree of increase of vessel stenosis (growth rate) caused by LDL deposition in the intima. Since in our model the growth rate due to LDL deposition relates linearly on the concentration of LDL at the inlet, we scaled the surface growth based on the actual culturing LDL concentration of 0.019 kg/ml. We predicted that at every medium change, after 30 min (1427 cycles) about all the perfused LDL would be adhering to the inner vessel surface without being removed, and that at the end of the 3 days of culturing before the subsequent medium change, the inner vessel surface growth would be of about 0.143 μm while at the end of the 4 weeks of modeling would be of 1.05μm (Figure 3c, d).The computational fluid-dynamics model identified possible intra-vessel, athero-susceptible regions at the vessel inlet, in a region affected by flow separation generated by an obstacle (silicon spacer). The obstacle divided the medium stream towards the vessels in two separated currents, leading to a local increase of flow velocity at the top and bottom of the vessel inlet (up to 0.15 m/s; Figure 3b), and to an drop in velocity at the sides (down to about 0.03 m/s; Figure 3b). Such regions were characterized by low wall shear stress (WSS) values spanning from 0.2 to 0.4 Pa, by the formation of whirlpools and vortices, any by a predilection for accumulating LDL particles (Figure 3d,e). Interestingly, the flux of passive scalar at the outlet did not allow for LDL particle massive deposition (Figure 3d) suggesting the presence at the inlet of each vessels of a putative atheroprone environment recapitulating the hemodynamic at the plaque region.

We developed an *in vitro* setup mirroring the CFD modeled conditions, aiming at verifying the predictions obtained *in silico* (Figure 3k). As a crucial step to model atherosclerosis on-a-chip, we developed a reproducible and consistent source of monocytes, key players in the disease to perfused through the bioengineered vessels. To do so, we first differentiated macrophage precursors (Mp) from iPSCs (Figure 3 j, Supplementary figure 6 a).

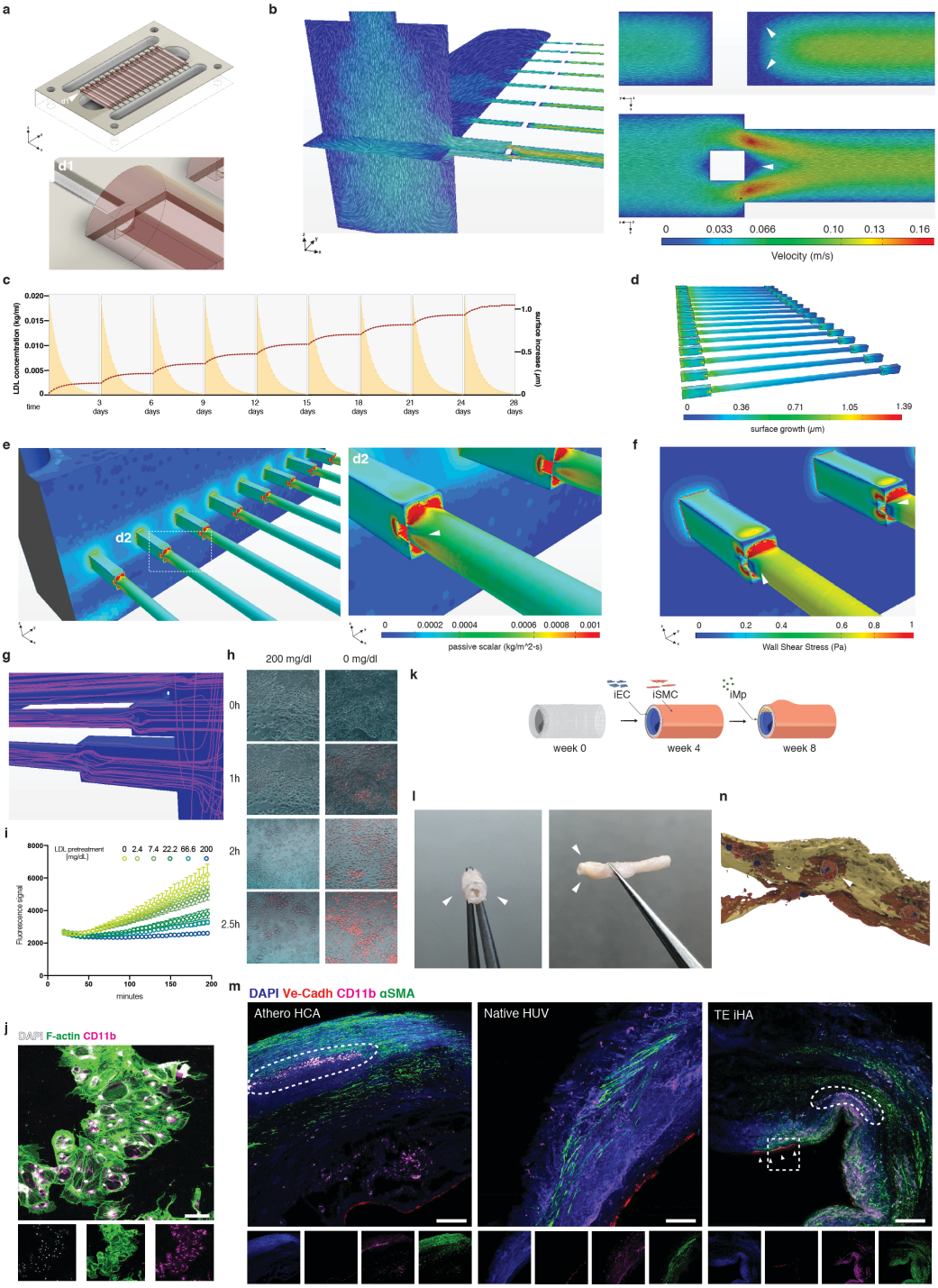

Figure 3. *in silico* and *in vitro* modelling of atherosclerotic plaque deposition. (a) CAD model showing the fluidic device loaded with tissue engineered vessels (in pink). A detail of a vessel inlet (d1). (b) Flow velocity within the device and at the vessel inlets from different perspectives. Vortexes and whirlpools are indicated by the arrow. (c) CDF prediction of LDL accumulation and increase in the luminal surface over time (28 days). Concentration of LDL perfused through the device over time (yellow), spiking at every medium change. Prediction of inner surface area increase during the modeling time (red dotted line). The first 1500 bioreactor cycles upon medium change are reported in the figure. (d) surface growth at the end of the 28 days of modelling time. (e) accumulation of LDL (passive scalar at the inlets) and a close-up detail (d2). (f) WSS at the inlets. (g) Modeled hypothetical tracks of the LDL particles through the device (purple lines). (h-i) Mp uptake of PhHRodoRed over time. (j) IF characterization of Mp from hiPSCs differentiated into macrophages. Scale bar 100µm (k) TE and modeling strategy. (l) TE vessels after 4 weeks of modeling. The arrows indicate regions of plaque accumulation. (m) Immunohistochemistry comparison of carotid arteries form patients' samples (Athero HCA), Native human umbilical veins (Native HUV), and tissue-engineered arteries from iPSCs (TE iHV). L = lumen, I = intima layer, M = media layer, S = scaffold remains. Scale bars 200µm. Round boxes = CD11b+ aggregates. Arrows indicate regions where CD11b+ cells adhere to the inner vessel wall of TE iHA. CAD reconstruction of the highlighted square region in Figure 3n. (n) CAD reconstruction from confocal imaging. Tissue engineered vessels showing Mp (cell body in dark red, nuclei in blue) adhering to the inner vessel lumen (Ve-Cadh signal in light brown).

The differentiated Mp, showed a transcription profile similar to the THP-1 monocytic/macrophage cell line, that was significantly different from the transcription profile of iPSC. Mp, showed a downregulation of pluripotency genes as *OCT4* ($p < 0.001$), *NANOG* ($p < 0.001$), *SOX2* ($p < 0.001$) concomitant with an upregulation of monocyte-macrophage lineage specific genes (CD36 $p = 0.03$, MSR1 $p = 0.03$) (Supplementary figure 6d). We then characterized the surface antigen expression profile of the Mp from factories at different timepoints using flow cytometry (Supplementary figure 6b, c). Within Mp we identified 10 different cell clusters, 3 of which were over-represented in Mp at each timepoint and characterized by pro-inflammatory monocytes/macrophages expressing $CD14^{high}$, $CD16^{high}$, $CD11b^{high}$ (Mo pro-inf 1, 14.2% ± 6.8, and Mo pro-inf 2, 42.2% ± 9.1), or by macrophages being $CD14^{low}$, $CD16^{high}$, $CD11b^{high}$ (Mf 1, 40.8% ± 12.6) (Supplementary figure 6 b,c). For our modeling experiments, we chose to use Mp isolated from 2 weeks-old Mp factories, as these Mp showed a higher percentage of pro-inflammatory monocytes/macrophages when compared to other culturing timepoints (Mo pro-inf 1, 20.5 %, and Mo pro-inf 2, 51.3 %). To test the ability of the iPSC derived Mp to become functional macrophages we differentiated the cells for 7 days. Upon differentiation, Mp adhered to the culture flask and developed a large cell body, positive for the CD11b immunostaining (Figure 3j). Adhesive macrophages were also able to uptake LDL in a dose-dependent way until temporary receptor saturation upon pretreatment with 200 mg/dl LDL (Figure 3h, i; Supplementary video 3).

To establish the atherosclerosis model on-a-chip, we perfused tissue engineered iPSC-derived arteries with syngeneic iMp form 2 weeks-old iMp-factories and for a period of 4 weeks (28 days). 500'000 iMp/ml were added at every medium change to the culturing medium in concomitance with LDL at high concentrations (ApoB100 200 mg/dl), in order to mimic a pro-inflammatory and hyperlipidemic state known to promote atherosclerotic plaque development (Figure 3k). At the end of the disease modeling time, we observed the formation of localized bulges at the vessel inlets, resembling the macro-anatomy of an atherosclerotic plaque (Figure 3l). We investigated whether such plaque-like structures included $CD11b^{+}$ macrophages allegedly differentiating from the perfused iMp,and migrating in the sub-endothelium. We showed that iMp in the pulsatile stream, adhered to the endothelial lumen (Figure 3m-n, Supplementary figure 6e), and migrated within the intima layer, gathering in $CD11b^{+}$ intra vessel cell aggregates (Figure 3m). Such cellular aggregates were not observed in non-treaded controls

(Supplementary figure 7) nor in native healthy vasculature (Figure 3m, Native HUV). Whereas, similar gathers were identified in atherosclerotic carotid artery explants (Figure 4m, Athero HCA). In LDL-/Mp+ controls we observed CD11b+ cells collecting at the lumen surface and eventually invading the tissue. However, such CD11b+ cells were not congregating in the inner vessels nor colocalizing with bulging areas (Supplementary figure 7). Additionally, LDL+/Mp- and LDL-/Mp- treated hiTEV controls appeared overall thicker than LDL-/Mp+ treated controls in CFD predicted plaque regions, hinting that Mp might have a crucial role in scaffold degradation and ECM remodeling during neo-tissue formation. Taken together, these observations provide the *in vitro* evidence that atherosclerotic plaque deposition is a process driven by a combination of pro-inflammatory and hyperlipidemic state in an atheroprone fluid dynamic environment and that such process is orchestrated by the phagocytic ability of macrophages gathering in the sub-intima. Importantly, our multifaced approached enabled the *in vitro* modeling of a desease-long *in vivo* process within a reasonable time frame.

3. Hierarchical consensus clustering algorithm identifies atheroma signature cell populations in modeled and native plaques versus healthy controls.

To validate our model, we compared plaque-resident cell populations isolated from tissue engineered models to cell populations from human native explants. We adopted a multiparameter flow-cytometry approach and a post-processing data analysis pipeline involving unbiased flow cytometry data normalization and gating, based on hierarchical consensus clustering algorithms. First, we investigated the changes in population abundance between native healthy and diseased explants. We found that late-atherosclerotic lesions had proportionally less myofibroblasts ($p = 0.04$), CD11c+ myofibroblasts ($p = 0.04$), smooth muscle and endothelial cells ($p = 0.03$) when compared to their healthy counterpart. However, late-lesion showed proportionally more dendritic cells specialized in antigen presenting tasks and in scavenger behavior ($p = 0.05$) (Figure 4a, c, Supplementary figure 8). Second, we compared healthy native explants to healthy tissue engineered specimens isolated from outlet sections of LDL+/Mp+ treated vessels. Such vessel-outlet specimens were not affected by tissue hyperplasia upon visual inspection at the end of the modeling time and were henceforth chosen as internal negative controls of plaque deposition (Figure 4b). Importantly, we found no significant differences between healthy native and tissue engineered specimens amid the analyzed populations (Figure 4a, c). Third, we compared the population abundances between tissue engineered atherosclerotic plaques and healthy tissue engineered samples. We found that the modeled tissue engineered lesions had proportionally less myofibroblasts ($p = 0.04$), CD11c+ myofibroblasts ($p = 0.09$) than the internal healthy control, but significantly more dendritic cells specialized in antigen presenting tasks ($p = 0.05$). Hence, when we compared native and tissue engineered lesions, we found similarities in population abundances of antigen presenting dendritic cells (ns, $p = 0.27$), endothelial cells with a scavenger phenotype (ns, $p = 0.68$) and macrophages (ns, $p = 0.10$). However, native lesions showed higher overall abundance of scavenger dendritic cells ($p = 0.04$) (Figure 4a, c). Our results indicate that the model developed in this study not only recapitulates key macro anatomical cues of the disease, but also allows for an accurate mimicry of the cell populations involved in plaque development.

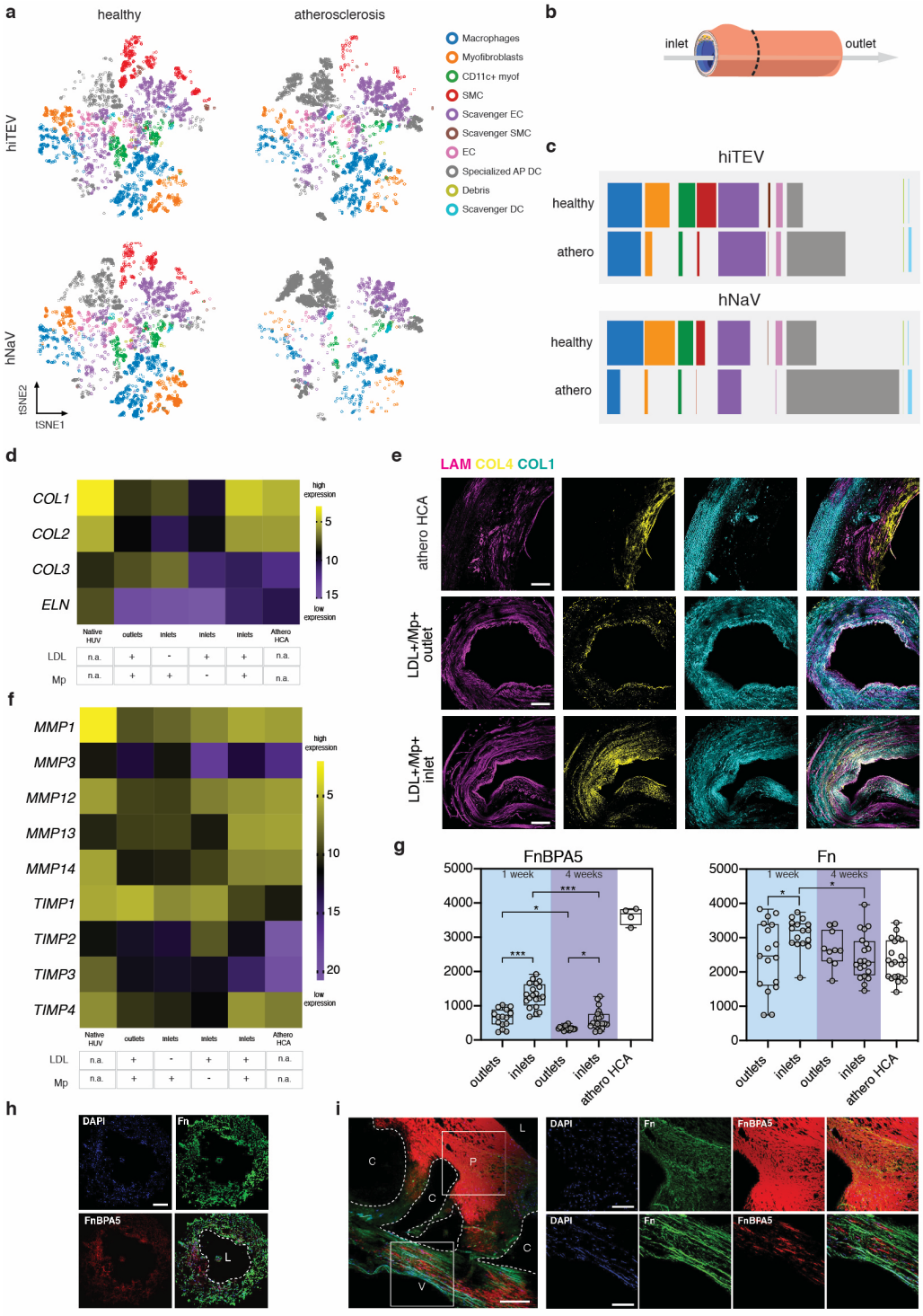

Figure 4. Cellular and extracellular characterization of modeled atherosclerotic plaques in hiPSCs-derived small-caliber arteries. (a). 2D t-SNE plots displaying relative populations' abundance from multiparameter flow cytometry data. Cell populations in healthy tissue engineered hiPSC-derived small-caliber vessels (hi-TEV) and human native healthy vasculature (h-NaV) are compared to their diseased (modeled or native) counterpart. (b) Overview of the tissue engineered vessel regions analyzed and compared in this study. (c) Display of relative population abundances in healthy and diseased hi-TEV and H-NaV. (d) RT-qPCR of Collagens and elastin in hi-TEV and native tissues (Native HUV, Athero HCA). (e)I mmunofluorescence analysis of spatial targeted ECM components. Atherosclerotic-like regions after disease modeling in hi-TEV (LDL+/Mp+ inlet) are compared to their internal negative control (LDL+/Mp+ outlet). Atherosclerotic regions from carotid artery explants serve as positive controls (athero HCA). Scale bars 200µm. (f) RT-qPCR of genes involved in ECM catabolism: matrix metallo proteinases (MMPs) and tissue inhibitors of matrix metallo proteinases (TIMPs). (g) Fn-BPA5 binding (red) in modeled tissue engineered vessels at the atherosclerotic plaque-like structure (LDL+/Mp+ inlets) vs regions in the same vessels without atherosclerotic plaque-like structures (LDL+/Mp+ outlets). Counterstaining of fibrillar fibronectin (green) in the same specimens. (h) ECM distribution of Fn-BPA5 (red) and fibrillar fibronectin (green) in a dissected plaque-like region from tissue engineered atherosclerosis model and (i) in a native carotid plaque. P = atherosclerotic plaque, C = former calcified regions, V= vessel media, L = lumen. Scale bars 200µm.

4. Transcriptional profile of ECM homeostasis, and Fn-BPA5 peptide binding patterns provide a signature of increased extracellular matrix remodeling in engineered plaques.

To explore the extracellular matrix landscape of the modeled tissue engineered plaques we investigated the transcriptional profile of classical ECM related genes which provided information on matrix remodeling within the targeted specimens. First and foremost, as expected, we found higher collagen type 1 (p = 0.007), type 2 (p = 0.02) and elastin ($p < 0.001$) transcript abundance in native healthy tissues, when compared to tissue engineered healthy specimens (hiTEV outlets) while no differences were observed for collagen type 3 (p = 0.49) (Figure 4d, Supplementary Table 1). Importantly, tissue engineered modeled specimens differed between diseased (LDL+/Mp+ hiTEV inlets) and healthy specimens (LDL+/Mp+ hiTEV outlets) in both collagen and elastin content. In detail, modeled plaque-like structures harvested at the inlets had less transcripts for collagen type 1, type 2 and elastin (p = 0.04, p = 0.03, $p < 0.001$ respectively) in comparison to their healthy counterpart, hinting to a possible downregulation effect on collagen type 1 and 2 exerted by Mp and LDL in combination with the peculiar flow dynamics of the inlet regions. To investigate this hypothesis, we dissected the ECM remodeling contribution in Mp-alone and by LDL-alone control treatments. We found that the treatment with LDL alone, had a stronger downregulation effect on collagen and elastin genes at the inlets compared to the combination LDL+/Mp+ in the same region (*COL1* p = 0.004, *COL2* p = *0.03, ELN* p= *0.01*), but LDL treatment did not impair *COL3* transcriptional levels. In contrast, Mp treatment alone lead to an upregulation of *COL3* (p= *0.04)* when compared to LDL+/Mp+ inlets, suggesting that the presence of Mp alone might contribute to the cellular population secreting collagen type 3, while LDL exerted an overall effect of gene downregulation. Importantly, the relative expression of genes for ECM anabolism from engineered and native plaques were comparable (*COL1* ns p = 0.39, *COL2* ns p = *0.42, COL3* ns p= *0.38, ELN* ns p= *0.27*) (Figure 4d, Supplementary table 1). Despite the gene expression profile indicating no differences in expression levels of collagen type 1, we observed a differential pattern of collagen fiber localization between native and tissue engineered lesions (Figure 4e). Collagen type 1 fibers were indeed globally distributed within the tissue engineered lesions with a preferential localization at the sub-intima, partially colocalizing with collagen type 4 fibers, while in native plaques they were mainly extending in the media layer. Nonetheless, the patterning of collagen 4 fibers was

similar in native and tissue-engineered plaques indicating that our model can successfully recapitulate core ECM characteristics of late-stage lesions.

Second, we compared the gene expression profile of markers for ECM remodeling including matrix metalloproteinases (MMPs) and their tissue inhibitors (TIMPs) (Figure 4f, Supplementary table 2, Supplementary table 3). We found that native healthy vessels had a higher abundance of *MMP1* ($p <$ 0.001), *MMP14* (p = 0.02), and *TIMP3* (p = 0.02) transcripts when compared to tissue engineered healthy specimens. We did not identify any other significant difference in other ECM remodeling markers between healthy native and tissue engineered vessels. Plaque-like structures from the modeled vessels showed lower *TIMP1* levels (p = 0.03), while exhibiting higher MMP13 (p = 0.04) relative transcript abundance. When we assessed the soloist role of LDL and Mp on ECM remodeling genes, we found that LDL had again a main effect on downregulation of gene expression, this time on *MMP3* (p = 0.03) when compared to healthy internal controls, while upregulating TIMP 2 (p = 0.05). Moreover, contrarily from what we expected, engineered vessels perfused with just Mp did not have any significant effect on ECM homeostasis. When we compared native plaques to modeled tissue engineered diseased specimens, we found *TIMP2* and *TIMP3* to be significantly downregulated within the engineered or native lesions ($p < 0.001$ in both cases). However, no additional differences were uncovered, indicating that our tissue engineered model may well recapitulate the ECM transcriptional profile of late-lesions.

Last, to further investigate the state of ECM remodeling upon 4 weeks of disease modeling, we focused on the fibronectin (Fn) fibers, one of first and foremost assembled and remodeled ECM fibers within the tissues during development and inflammation. We hypothesized that the peculiar and dynamic flow environment would affect Fn remodeling both in native plaques and in our tissue engineered atherosclerosis model. To test our hypothesis, we stained tissue engineered vessels using a fluorescently labelled Fn-BPA5 peptide, previously described to be capable of binding to fibronectin fibers with a relaxed conformational state following exposure to low strain (Figure 4h, i). Such low-strain regions are particularly common in fibrotic and overly remodeled tissues[33]. We counterstained the samples with an antibody recognizing fibrillar fibronectin and further quantify pixel-by-pixel the intensity

of both components with confocal microscopy to extrapolate the ratio between total Fn and relaxed Fn fibers (Figure 4g). We found that the Fn-BPA5 peptide binds profoundly to the plaque-like structures developed within the vessel inlets upon modeling (LDL+/Mp+ inlets) already after 1 week compared to the control group (LDL+/Mp+ outlets) ($p < 0.001$), and such difference in Fn-BPA5 persisted after 4 weeks of modeling ($p = 0.01$) (Figure 4g, Supplementary Figure 8). To provide a comparison with real-life late-lesion, we stained human carotid plaques using the same procedure described above. We observed for the first time that the Fn-BPA5 peptide selectively binds to plaque regions, indicting a prevalence of Fn fibers under low strain. Overall, our data indicate that the atheroprone modeling environment promotes a dynamic and profound reshuffling of ECM components within the tissues. The observations that atheroprone areas were richer in Fn-BPA5 than internal non-atheroprone regions, and that human late-lesions were positive for Fn-BPA5 staining in the hyperplastic area, support our hypothesis, endorsing the role of flow dynamic as a major player in Fn, and more in general, of ECM remodeling.

Discussion

Despite decades of research in the atherosclerosis research field, there are still profound unmet clinical needs that make it fundamental to elucidating the pathophysiology of plaque seeding (initiation), progression, rupture, stabilization, and regression[36] In this scenario, it is pivotal to develop human cell-based disease models with high translational relevance to dissect each step of the process, to understand and ultimately control disease progression. This work introduces a human plaque-on-a-chip in vitro model, first of its kind, entirely developed using healthy tissue-engineered vessels generated from syngeneic iPSC-derived cells. First, we differentiated and characterized human arterial endothelial cells and contractile smooth muscle cells from hiPSCs based on an adapted version of well-established protocols[37,38]. We then generated hiTEV with an inner diameter of 500 μm by establishing a novel VTE approach, which included a biodegradable PGA/P4HB-based scaffold and alternating static and dynamic culturing conditions using a novel microfluidic device connected to a customized bioreactor set up in a controlled fluid dynamic environment. Similar VTE approaches have been used to develop bioengineered large vascular conduits and heart valves that are now in clinical trial for the first-in-man applications[21-25]. The hiTEV obtained with our novel VTE method showed microanatomical architecture, layering, ECM components, and cell types comparable to human native arteries (small muscular arteries and arterioles). he hiTEV obtained with our novel VTE method showed microanatomical architecture, layering, ECM components, and cell types comparable to human native arteries (small muscular arteries and arterioles). Other VTE approaches have attempted to recapitulate the vascular anatomy using hiPSC-derived or native cells[16,39]. Despite the pioneering efforts, such previous approaches lack sufficient molecular and functional characterization of the adopted cells, convincing histological analyses of the tissues, and the description of a replicable culturing setup. Here we present a detailed portrayal of protocols, materials, fluidic devices, and culturing set up to overcome these issues, providing all the necessary information, including stl. files with the original design of the components of the microfluidic chamber.

Second, we developed a computational fluid-dynamic analysis that successfully predicted atheroprone, hyperplasic, LDL-laden inflammatory niches in hiTEV. The CFD model highlighted flow disturbances, whirlpools, and split flow regions as those more prone to long-lasting impact, therefore accumulation,

with LDL particles. These findings are in line with previous reports[18,40,41] and complemented our in vitro results upon perfusion of hiTEV for 28 days in atheroprone conditions with iPSC-derived macrophage precursors derived from the respective factories[42,43]. Notably, the formation of plaque-like structures was observed in LDL+/Mp+ treated hiTEV, but not in LDL-/Mp-, LDL-/Mp+ nor in LDL+/Mp- treated controls. Furthermore, we observed that macrophages could adhere to the luminal surface of LDL-/Mp+ treated hiTEV but did not gather in the intima nor media layer of the vessels. These findings support the observations that the process of Mp patrolling the vessel lumen is a part of regular cell physiological activity and that transmigration, hence plaque seeding observed in LDL+/Mp+ treated hiTEV, is triggered by intra-vessel LDL accumulation[44,45]. Our findings support the hypothesis that atherosclerotic plaque deposition is a process orchestrated by the phagocytic ability of macrophages gathering in the sub-intima and by shear-dependent blood-wall mass transport, providing provide a first in vitro evidence of such dynamic process[1,7,46-48].

Third, we analyzed the cell populations within the formed plaques using multiparameter flow-cytometry analysis with a novel, user-independent, hierarchical consensus clustering algorithm for unbiased data post-processing[49]. With this approach, we identified atheroma signature cell populations in modeled and native plaques different from healthy controls, enabling immune cell profiling of the human atheroma in both native and tissue-engineered specimens. These experiments revealed a close resemblance of our model to the cellular component of real-life late-stage human carotid plaques, adding to previous findings in the field [17,50]. Importantly, we found similarities between native and tissue-engineered lesions in population abundances concerning antigen-presenting dendritic cells, endothelial cells with a scavenger phenotype, and macrophages. However, native lesions showed a higher overall abundance of scavenger dendritic cells, in line with previous reports[17,51-53]. We then dissected and compared the extracellular matrix milieu of native and tissue-engineered plaques finding close resemblance in transcription levels of genes for ECM assembly and remodeling. Importantly, diseased specimens from hiTEV showed downregulation of elastin transcripts to levels similar to those found in native plaques and differently from what was observed in healthy native samples. Similar findings have been reported by previous in vivo studies on mouse models[54,55] . Here, a candidate micro RNA (miRNA 181b) overexpressed in human atherosclerotic plaques has been framed as the responsible candidate

for indirect downregulation of collagen and elastin deposition by vascular smooth muscle cell, by direct downregulation of MMP-3 at the transcriptionallevel[54]. Furthermore, we found similarities between native and bioengineered plaques concerning Fn-BPA5 peptide-binding patterns. The fn-BPA5 peptide was previously used to assess the tensional state of fibronectin fibers in tumors and virus-infected lymph nodes[33,56] . These studies reported the ability of Fn-BP5 peptide to bind to regions of fibronectin in a low tensile state. Here, we show for the first time the ability of the Fn-BP5 peptide to bind both to native and bioengineered plaque regions, providing a possible diagnostic mean and even a hint to the development of novel therapeutic tools to counteract local plaque accumulation. Overall, our findings provide an indication of increased fibronectin, collagens, and elastin remodeling in the engineered plaques and offer an unscalable platform to investigate ECM remodeling in atherosclerosis development and treatment.

The atherosclerosis on-a-chip model presented in this work aims at complementing and eventually reducing the use of animal models in atherosclerosis research, offering a human cell-based option with higher translational power. Importantly, so far, most of the small animal models (i.e., rabbit and mouse models) used in the field are genetically engineered or fed with lipid-rich diets to accumulate intra vessel plaques, despite harboring entirely different blood lipoprotein profiles when compared to human[57-60]. Large animal models as pigs and non-human primates provided significant advancements in the atherosclerosis research arena, especially concerning the study of hemodynamics in plaque development and positioning within preferential vascular regions[61-63]. Despite that, pre-clinical research using large animal models remains complicated, expensive, and accompanied by growing ethical concerns[61]. Several human cell-based three-dimensional models attempted to recapitulate and study the plaque microanatomy by investigating the interplay of the disease's primary cell players, as endothelial cells, macrophages, and smooth muscle cells separately[32,64,65]or together in multicellular models [16,17]. Other pioneering studies have focused on the effects of the hemodynamics and shear stress[66] and on the role of hyperlipidemia or inflammation in plaque progression[67]. So far, despite the need of the scientific community, no study has ever embraced such a holistic, multidisciplinary approach for the investigation and atherosclerotic plaque deposition[68].

Besides the advancements introduced by this model, it is important to mention that there are still

limitations to our approach. First, the flow-cytometry characterization and the qPCR analysis performed on hiPSCs-derived iECs, iSMCs, and macrophage precursors revealed these cells to retain a fetal like phenotype, a common characteristic of most hiPSC-derived cells that has been extensively described in literature[69]. However, it is important to mention that, contrary to common belief, atherosclerosis is a vascular condition "without age". Atherosclerotic plaques have been found in fetuses[70], children[71],and young adults[72]. Conversely, the disease consequences (i.e., plaque rupture, myocardial infarction) maintain a high prevalence in elderly subjects, mainly due to the presence of comorbidities exacerbating disease progress[73]. With this in mind, we believe the impact of the phenotypical cell age on the model output to be limited. Second, our model investigates intravascular inflammatory events mediated by macrophage precursors and does not include other cells that might interfere with the etiology of the disease in real-life (i.e., T and B cells)[74]. The choice to omit those cell types from the modeling setup was driven by the will to explore a minimalistic disease scenario to test the response-to-retention hypothesis of early atherogenesis[75], which we later confirmed. Third, our CFD model lacks an accurate rendering of the vascular component, herein considered as an inert element. The model could be improved in the future by including more informative boundary conditions based on data from mechanical testing experiments. Moreover, our computational model can be further enhanced in the future by implementing accurate finite element modeling (FEM) approaches. Such updates shall be based on two-way coupling computations, where the scattered LDL particles within the model are influenced by the system (i.e., medium flow) and by impacts with other particles within the device.

In conclusion, we suggest that our *in vitro* culturing setup, as well as the tissue-engineering and modeling strategy employed in this study, fosters the formation of a stratified, native-like arteriolar microanatomy and recapitulates key macro anatomical cues of the disease. Our model allows for an accurate mimicry of the cell populations involved in plaque development and of the profound pathophysiological rearrangement of ECM components in a controlled environment. Finally, this study shows how fruitful crosstalk between biology, medicine, and computational modeling can develop tools that can ultimately serve patients. In this regard, the implementation of CFD approaches is now on the rise in tissue engineering and personalized medicine[23]. CFD approaches strongly contribute to the development of novel, more accurate TE models, offering powerful tools to gather insights into the physiologic and pathophysiologic remodeling phenomena observed in atherosclerosis development but

not limited to this arena.

Materials and methods

1. Cell culture

1.1 Culture of human induced pluripotent stem cells. Two different induced pluripotent stem cell lines were used to conduct the tissue engineering experiments included in this work, HPSI0114i-eipl_1 (RRID:CVCL_AE06), WTB6 (RRID:CVCL_VM30), and were purchased from the European Bank for induced pluripotent stem cells (EBiSC). hiPSCs were thawed into 6 well plates (TPP) that were pre-coated for 1h at RT with 10 µg/ml Vitronectin (Stem Cell Technologies) in CellAdhere dilution buffer (Stem Cell Technologies). Each coated plate was prepared fresh before use. iPSCs were thawed in 1 ml of mTeSR medium (Stem Cell Technologies) with the addition of 10 µM Rho kinase inhibitor (ROCKi, Y-27632; Sigma). After 24h, and upon adhesion of the cells to the bottom of the well, the medium was replenished with mTeSR without ROCKi. The medium was refreshed every day after 1 washing step in DPBS (Gibco). The cells were constantly monitored for signs of differentiation such as the formation of uncompacted colonies, the presence of not-well defined colony edges, or variations in colony shape from the regular circular or oval morphology. iPSCs were passaged at about 70% confluence. At the right time, cells were detached using ReLeSR (Stem Cell Technologies) at 37°C for about 5 min. Afterward, mTeSR medium was added in a 1:1 ratio, and the detached cell aggregates were carefully transferred to a 50 ml (Falcon) tube using 5 ml pipettes to avoid the formation of single-cell suspensions. Generally, hiPSCs cultures were passaged every 4-7 days using either a 1:4 or a 1:6 split ratio.

1.2 Culture of endothelial cells. Human umbilical vein endothelial cells (HUVECs) were harvested from healthy specimens of umbilical cords donated to the Institute for Regenerative Medicine of the University of Zurich, within the work frame approved by the Kantonale Ethikkommission Zürich (KEK-Stv-21-2006). Briefly, umbilical cords were dissectioned and the umbilical vein was isolated, washed in PBS (Gibco) and infused with an enzymatic mix of collagenase/dispase (Sigma) for 20 min. At this point, the collagenase/dispase solution was collected in a 50 ml tube (Falcon), the umbilical veins were then rinsed in PBS and the washes were collected in the same tube containing the rinsed enzymatic solution. EGM-2 medium (Lonza) was added in a 1:1 ratio to the cell suspension before a centrifugation step at 300g for 5 minutes. HUVECs were pelletized, resuspended in EGM-2 medium and plated onto 0.1% gelatin-coated (Sigma) 6 well plates. The medium was refreshed every 2-3 days, after 2 washes

is PBS. HUVECs were sub-cultured at about 80% confluence in a 1:6 subculturing ratio. Human brain microvascular endothelial cells (HBMECs) were purchased from ScienCell Research Laboratories cultured, sub-cultured and processed as described for the HUVECs.

1.3 Fibroblasts and myofibroblasts. Human umbilical vein myofibroblasts (HUVMs) were harvested from healthy umbilical cords donated to the Institute for Regenerative Medicine of the University of Zurich, within the work frame approved by the Kantonale Ethikkommission Zürich (KEK-Stv-21-2006). Briefly, umbilical cords were dissectioned and the umbilical vein was isolated, washed in PBS and cut in pieces of 1mm × 1mm size. Vein wall fragments were then scattered onto a 10cm Petri dish (TPP) and let adhere to the bottom of the plate for 15 min before the addition of DMEM medium, that was prepared as follows: 10% FBS (Gibco), 1% Glutamax (Gibco) and 1% Penn Strep (Sigma) in DMEM medium (Sigma). After about 10 days, myofibroblasts were sprouting from the tissue fragments forming a 60% confluent layer. Here, cells were detached from the dish using Trypsin – EDTA solution 0.025% (Sigma), washed in PBS and sub-cultured at a 1:3 ratio. The DMEM medium was refreshed every 2-3 days, after a wash in PBS. HUVMs were passages at 80% confluence. Human aortic fibroblasts (HAFs) were purchased from ScienCell Research Laboratories and processed as described for HUVMs.

2. hiPSCs differentiation

2.1 Differentiation of hiPSCs to arterial endothelial cells. hiPSCs were differentiated to arterial ECs via mesodermal lineage control performed with VEGF and cyclic AMP, following an adapted version of the protocol published by T.Ikuno *et al.*[76]. In detail, hiPSCs colonies were disaggregated to single cells and plated onto freshly prepared thin-coated Matrigel (Corning, 1:60) plates at a density between 60'000-80'000 cells/cm^2 (Day 0). Cells were cultured for 72h in mTeSR™ medium enriched with 4ng/ml FGF-B. (Gibco). At this point, the differentiating cells were further coated with a thin layer of Matrigel (1:60) and after 24h, the medium was replaced with RPMI1640 medium (Sigma) enriched with 2mM Glutamax, 1×B27 supplement minus insulin (Gibco), and 125 ng/ml activin-A (PeproTech). After 18h, the medium was replaced with RPMI1640 medium enriched with 2mM Glutamax, 1XB27 supplement minus insulin, 10ng/ml BMP-4 (Sigma), 10 ng/ml FGF-B and Matrigel (1:60). On Day 8, the medium replacement was performed with RPMI1640 plus 2mM Glutamax, 1×B27 supplement minus insulin, 1mM 8bromo-cAMP (Stem Cell Technologies) and 100ng/ml VEGF-A (ThermoFisher). On Day 11, the differentiated

CD144+ endothelial cells were magnetically sorted on MACS separation columns (Myltenyi Biotec) and seeded at a density of 10'000 cells/cm^2 on thin-coated, Matrigel dishes in RPMI1640 medium enriched with 2mM Glutamax, 1×B27 supplement minus insulin, 1mM 8bromo-cAMP , 100ng/ml VEGF-A and 10 µM ROCKi. On day 14, the medium was replaced with arterial specification medium prepared as follows: EGM-2 medium with 1mM 8bromo-cAMP. The arterial specification medium was refreshed on day 16 and the resulting arterial endothelial cells were harvested at day 19. ECs were cultured in EGM-2 medium and transferred onto 0.1% gelatin coated dishes at a seeding density of 10'000 cells/cm^2. Induced pluripotent stem cells-derived arterial endothelial cells were passaged at a confluence of about 80%.

2.2 Differentiation of hiPSCs to contractile smooth muscle cells. hiPSCs were differentiated towards contractile smooth muscle cells using an adapted version of the protocol proposed by Yang *et al.* [38]. In detail, hiPSCs were pushed towards the mesodermal lineage by replacing the regular hiPSCs culturing medium mTeSR™ with mesodermal medium prepared as follows: 5µM CHIR99021(Stem Cell Technologies), 10ng/ml BMP-4, and 2% B27 with insulin (Gibco) in RPMI1640 medium (Day 0). On day 3, the medium was replaced with RPMI1640 enriched with 25 ng/ml VEGF-A, 25 ng/ml FGF-B and 2% B27 minus insulin. The medium was refreshed on day 5. On day 7, the medium was replaced with RPMI1640 medium enriched with 5ng/mL PDGF-B (Stem Cell Technologies), 2.5 ng/mL TGF-B (PeproTech), and 2% B27 with insulin. A medium refreshment was performed every second during the day the following six days. On day 14, the contractile SMCs were selected by culturing the cells in RPMI1640 with 4mM lactate (Sigma). On day 20 the cells were harvested for further characterization or sub-cultured in SMC medium prepared as follows: 5% FBS, 2mM Glutamax, 5ng/mL PDGF-B, 2.5 ng/mL TGF-B in DMEM F12. The cells were passaged at 80% confluence and seeded at a seeding density of 10'000 cells/cm^2.

2.3 Differentiation of hiPSCs to macrophage precursors. hiPSCs were differentiated to macrophage precursors (iMp) following the protocol adapted from Haensler *et al.* [43] and van Wilgenburg *et al.*[42]. In detail, 4 million hiPSC were seeded into an AggreWell 800 well (Stem Cell Technologies) according to the manufacturer's instructions to generate embryoid bodies (EBs), using E8 medium (Stem Cell

Technologies) and fed daily with medium supplemented with 50 ng/mL BMP-4, 50 ng/mL VEGF, and 20 ng/mL SCF (PeproTech). After 4 days, EBs were collected and used to setup macrophage factories in T75 flasks (75 EBs/flask) or T175 flasks (150 EBs/flask) in X-Vivo15 (Lonza), supplemented with 100 ng/mL M-CSF (PeproTech), 25 ng/mL IL-3 (PeproTech), 2 mM Glutamax, 1% penn/strep solution, and 0.050 mM β-mercaptoethanol (Gibco). Fresh medium was added once per week. iMp emerged into the supernatant after approximately 3 weeks of differentiation and were collected weekly. Upon collection, iMp were passed through a 40 μm cell strainer (Corning) to obtain a single cell suspension and were either plated onto tissue-culture treated at a standard density of 100'000 per cm^2 and differentiated for 7 days to macrophages in X-Vivo15 supplemented with 100 ng/mL M-CSF, 2 mM Glutamax, 1% penn/strep solution for mono-culture assays (i.e., LDL uptake assay), or resuspended in perfusion medium and added to the organ on-a-chip model.

3. hiPSCs functional characterization

3.1 Tube formation assay - characterization of iECs. Tube formation assay was performed following an adapted version of a previously described protocol [76]. Specifically, 10'000 differentiated ECs at day 19 were plated on μ-Slide Angiogenesis (Ibidi) in 10 μl of Matrigel/well in EGM-2 medium and imaged at time point 0 and after 24h. HUVECs and HBMECs were used as controls cell lines.

3.2 Gel contraction test - characterization of iSMCs. SMCs derived from hiPSCs were suspended (2.5×10^5 cells) in 60µl of an 8 mg/ml fibrinogen solution (Sigma). Hence, the fibrinogen cell suspension was mixed with 60 µl of a 5 U/mL thrombin solution (Sigma) and carefully but quickly deposited in the center of a well of a 24 well plate (TTP) and incubated at 37°C for 10 min in order to allow the complete hydrogel polymerization. The gels were cultured in 1 ml DMEM medium containing 5% FBS, 300 U/ml aprotinin (Sigma) to prevent hydrogel size reduction due to fibrinolysis, and 10 µM ROCKi. Gel sizes were measured at day 0 and at day *3*. HUVMs and HAFs served as controls cell lines.

3.3 Wound healing assay - characterization of iSMCs. SMCs derived from hiPSCs (4×10^4cells) were resuspended in 140µl of DMEM medium containing 5% FBS and 2 mM Glutamax. The cell suspension was distributed in two silicon cell culture reservoirs of a 24-well plate culture-insert (Ibidi) positioned in

the wells of 24 well plates. After 2h, upon full cell adherence to the bottom of the plate, the medium was refreshed. After 24 hours, the medium was further replaced with DMEM medium containing 1% FBS and 2 mM Glutamax, and the silicon inserts were removed to allow cell migration. Plates were imaged with a microplate reader (Tecan, SPARK® multimode) and cell migration was reported at 0h and 48h post serum starvation. HUVMs and HAFs served as control cell lines.

3.4 LDL uptake - characterization of iMp. Macrophage precursors derived from hiPSCs SFC840-03-03, SFC854-03-02, SFC856-03-04 (previously characterized [77,78]), HPSI0114i-eipl_1 and WTB6, were seeded at a density of 100'000 cells/cm^2 in 96-well flat clear bottom black tissue culture plates (Corning), and differentiated for 7 days in XVivo-15 medium enriched with 100ng/ml M-CSF, 2mM Glutamax and 1% penn/strep solution. Labelled low density lipoprotein, pHRodoRed-LDL (Invitrogen) was applied at a concentration up to 2.5 μg/ml in Life Imaging buffer (Gibco). Fluorescent images were acquired with an EVOS M7000 imaging system, supplied with an on-stage incubator unit that was set to 37°C. Cells were imaged over 3 hours after pHRodoRed-LDL treatment. Fluorescence intensity was also monitored with fluorescence plate reader (Tecan, Infinite M1000pro), heated to 37°C. 4 reads per well were acquired, every 5 min for 3 h and the mean value was used for further analysis. The fluorescence plate reader was set to excitation wavelength of 560 nm, 10 nm bandwidth, and emission wavelength to 585 nm, 15 nm bandwidth. For LDL uptake inhibition, cells were pre-treated with different concentrations of unlabelled LDL for 30 min (LeeBio), then the medium was removed and directly replaced with life Imaging buffer containing pHRodoRed-LDL.

4. Native tissue specimens

Biopsies of human umbilical veins were obtained from umbilical cords donated for research purposes from healthy subjects in accordance to the ethical protocol approved by the Kantonale Ethikkommission Zürich (KEK-Stv-21-2006). Participants have been informed about the research project before the tissue retrieval and the consent has been be sought from each participant. No compensation was provided to the donor subjects. The sample retrieval was performed during a common clinical procedure therefore, no additional risks for the patient were present. Biopsies of carotid branches were obtained from patients undergoing scheduled carotid endarterectomy and shunting, secondary to vascular stenosis in accordance with the protocol approved by the Ethik Kommission der Universität

Witten/Herdecke (Nr.79/2012). Inclusion criteria: age ≥ 18 years old, being scheduled to undergo a carotid endoarterectomy. Exclusion criteria: malignancy, liver failure, renal failure (Creatinine >180 ug/ml), hereditary coagulation disorders, anemia (Hb < 10 g/dl), Rheumatic heart disease, Rheumatoid arthritis.

5. RT-qPCR

5.1 RNA extraction. For RNA extraction the RNeasy Mini Kit (Qiagen) was used. In case of extraction from adherent cell cultures, the lysis buffer RTL with 10 µl/ml β-mercaptoethanol (Sigma) was directly applied to the culturing plate, the solution was collected in low-bind PCR tubes (Eppendorf) and stored at -80°C until further processing. In case of RNA extraction from native tissues or hiTEVs, the tissues were disrupted in a tissue lyser (TissueLyser II, Qiagen) with 3 mm tungsten beads (Qiagen) in a RTL solution with 10 µl/ml β-mercaptoethanol and the tubes were stored at -80°C. The isolated RNA was measured with a spectrophotometer (NanoDrop 2000, Thermo Scientific) and immediately processed for reverse transcription.

5.2 Reverse transcription. The reaction was performed for each sample in a final volume of 20 µl reaction mix containing 1 µg of RNA, 1 × PCR buffer, 5mM $MgCl_2$, 10 mM dNTPs, 0.625 µM oligo $d(T)_{16}$, 1,875 µM random hexamers, 20 U RNase inhibitors and 50 U MuLV reverse transcriptase (ThermoFisher). The thermocycler settings were as follows: 25 °C for 10 minutes, 42 °C for 1h, followed by 99 °C for 5 minutes. The resulting cDNA was either processed immediately, stored at 4 °C for a maximum of 48h, or transferred at -20 °C for long term storage.

5.3 Quantitative real-time PCR (qPCR). The reaction was performed for each sample in a final volume of 10 µl reaction mix containing 30 ng of cDNA, a 1:1 mix of froward and reverse primers in a final concertation of 100nM and FAST SYBR green (ThermoFisher). The primers for each tested gene are summarized in the Supplementary table 4. The qPCR was performed on StudioQuant7 (Applied Biosystems) and the amplification program was set as follows: 95° C for 5 min, 40 cycles with 95 °C for 10 seconds, 60 °C for 15 seconds, 72 °C for 20 seconds. The software QuantStudio 6 and 7 Flex Real-Time PCR System (Version 1.0) was used for data acquisition. Gene expression levels were normalized over the two housekeeping genes (HKG): the glyceraldehyde 3-phosphate dehydrogenase (*GAPDH)*

and the small subunit 18S ribosomal RNA (*18S)*.

6. Immunofluorescence analysis

6.1 Fixation and staining. Cells grown in 2D cultures were fixed in 4% cold paraformaldehyde (PFA, Sigma) for 20 minutes at RT. Tissues from native specimens and hiTEVs were embedded unfixed in OCT matrix (Tissue-Tek®) and transferred onto dry ice to allow water-soluble glycols and resins to solidify. Hence, the samples were processed in a cryostat (Tissue-Tek®) and shed in slices of 5 μm thickness. For the immunofluorescence staining, cells and tissue sections were washed twice in PBS, flowed by permeabilized with 0.2% Triton-X 100 (Sigma) in 1× PBS for 10 min RT and blocked in 1%BSA (Sigma), 0.1% Tween-20 (Sigma) in 1× PBS for 20 min RT. Hereafter, the cells were incubated with the primary antibody for 1h at 37 °C, washed three times in 1× PBS, and stained with secondary antibodies for 1h at 37 °C. The specifications concerning the antibodies used for IF are collected in the Supplementary table 5. After secondary antibody staining, the samples were washed three times and counterstained with DAPI 0.2 μg/ml (Sigma) and mounted in Vectaschield® (Vector Laboratories).

6.2 Confocal microscope imaging and analysis. The stained specimens were analysed with a confocal microscope (Leica TCS SP8) where images were acquired as z-stacks. The acquisition speed was set to 400 Hz, and the picture size to 1024 × 1024 pixels. Each acquired image of the z-stack composite was the result of an average of 10 acquired frames from the same region. The data were then processed using the software ImageJ Fiji (Version 1.52p Java 1.8.0_172 64-bit). The z-stacks from individual positions within the 2D cell culture or 3D tissue were summarized in one image collecting the maximum intensity voxels from different planes of focus. Each acquired channel was singularly processed as described in the previous sentence and a composite image was created as a merged version of the channels of interest.

7. Flow cytometry

7.1 Generation of single cell suspensions from tissue-culture vessels, human tissue and control samples. Native vessels and TEVs were cut into small pieces of about 1mm × 1mm, collected into small 1.5 tubes (Eppendorf) and digested at 1200 rpm in a tube shaker (Eppendorf) in a solution with 1 mg/ml

collagenase/dispase, and 0.5 mg/ml Dnase in 1 × HBSS with Ca^{2+} and Mg^{2+} for 30 min at 37 °C. Single cell suspensions were filtered through 70 µm nylon meshes (BD Biosciences) and washed in HBSS. Frozen peripheral blood mononuclear cells (PBMCs) isolated from donor blood samples provided by the Zurich Blood Bank (Blutspende Zürich, project Nr.6676) were used as control samples, together with pooled macrophage precursors from HPSI0114i-eipl_1 and WTB6 factories. 2D monocultures of HUVECs and HUVMF were also used as controls and were thawed at 37°C and washed twice in PBS at RT before further processing.

7.2 Atheroma signature cell population processing, antibody panel and acquisition. Single-cell suspensions were incubated for 30 min at 4 °C in Zombie Aqua live/dead exclusion dye in HBSS without Mg^{2+} and Ca^{2+}, (LIVE/DEAD™ Fixable Aqua Dead Cell Stain Kit, Molecular Probes, Thermo Scientific). Next, cells were washed in FACS buffer prepared with 2% (v/v) heat inactivated FBS, 5 mM EDTA, 0.01% (v/v) NaN_3 (Sigma) and resuspended in Fc receptor blocking antibodies (1:20 from stock in FACS buffer, anti-mouse CD16/32 TruStain fcX, Biolegend). After 5 min incubation, cells were treated with antibody master mix for surface marker staining and incubated for 15 min at 4 °C, followed by a last wash in FACS buffer. For identifying atheroma signature cell populations we used following fluorophore-conjugated antibodies against targeted surface markers (Supplementary Table 5). For intracellular staining, cells were fixed and permeabilized according to manufacturer's instructions (Fixation/Permeabilization and Permeabilization Buffer, eBioscience, Thermo Scientific). Cells were incubated with antibody master mix in 1x Permeabilization buffer for 30 min at 4 °C and incubated with the following fluorophore-conjugated antibody: Alexa Fluor647 anti-αSMA (1:80, clone, company). Fluorescence-minus-one (FMO) samples were included as negative controls. Cells were acquired on a 16-channel LSR II Fortessa flow cytometer (BD Biosciences).

7.3.Data cleaning. Via FlowJo (Version 10.0.8, FLOWJO LLC) software, the forward and side scatter signal of every sample was used to exclude any low-size debris and cell-doublets. Furthermore, Zombie Aqua live/dead exclusion dye-positive dead cells were cleaned out. For follow-up analyses we pre-selected all living cells.

7.4 Data normalization, visualization and automated clustering. Living-cell data was normalized via Gaussian Normalization Function in R (gaussNorm, version 3.6.1, R Core Team) implemented in RStudio user interface (version 1.1.447, RStudio, Inc.). Using the viSNE function of the online database Cytobank (https://cytobank.org/cytobank, Cytobank, Beckman Coulter), the multi-parameter n-dimensional data was processed by nonlinear dimensionality reduction tSNE algorithm (t-distributed stochastic neighbor embedding algorithm), in order to visualize cell populations in a two-dimensional space, called viSNE plot (settings: 2500 iterations, 30 perplexity). In order to increase sample size for better visualization in viSNE plots, we concatenated all samples of each experimental group a priori via flowCore (R package version 1.44.2, DOI: 10.18129/B9.bioc.flowCore) and Premessa (R package version 0.2.4, https://github.com/ParkerICI/premessa).Automated, unsupervised cell subpopulation clustering was obtained by FlowSOM (self-organizing maps for flow data) analysis, using the hierarchical consensus clustering method (settings: 10 metaclusters, 10 iterations) of Cytobank (https://cytobank.org/cytobank, Cytobank, Beckman Coulter). The automatically identified clusters were overlaid with their corresponding cell events in the viSNE plots, quantified and exported to GraphPad Prism (Version 9.0, GraphPad Software) for statistical analysis.

8. Tissue engineering of small-caliber tissue engineered arteries

8.1. Tissue engineering, microfluidic device and bioreactor setup. Non-woven polyglycolic acid (PGA) meshes (thickness 1 mm; specific gravity 70 mg/cm^3; Cellon) were coated with 1.75% poly-4-hydroxybutyrate (P4HB; TEPHA, Inc., USA) by dipping into a tetrahydrofuran (THF) solution (Sigma). After solvent evaporation and drying overnight, the scaffolds were shaped as small conduits of length 1.5 cm with an inner diameter of 500 μm. 48h before cell seeding the constructs were placed into 80% EtOH (Sigma) for 30 min, washed twice in 1× PBS and incubated in SMC medium (See *Materials and Methods section 2.2*) overnight to facilitate cell adherence. hiPSCs-derived SMCs were seeded within the PGA tubular scaffolds at a seeding density of 6 × 10^6 cells/cm^2 in a seeding volume of about 1.5 ml/vessel. 750μl of fibrinogen (Sigma) (10 mg/mL of active protein) and 750μl thrombin solutions (Sigma) were prepared. iSMCs were resuspended in the fibrinogen-thrombin mix and distributed both in the inner lumen and the outer surface. After 10 min, that were necessary for hydrogel crosslinking,

the seeded constructs were moved in iSMC- culturing medium enriched with 0.9 mM of l-ascorbic acid-2-phosphate (Sigma)(Day 0). At day 2 the medium was replaced with plain iSMC-culturing medium and the constructs were maintained in static culture untill day 7. The microfluidic device was built through computer numerical control (CNC) guided milling of aluminum and poly methyl methacrylate (PMMA) and silicon (VMQ), performed at the department of physics of the ETH Zurich (Switzerland) and was designed to host the simultaneous culture of 16 hiTEVs, to facilitate access to the cultured specimens, opening and closing operations, and to be reused for multiple times. The microfluidic device components were disassembled, thoroughly cleaned, washed in EthOH 80% overnight and sterilized under UV light for 2h. At day 7, tissue engineered constructs were moved within the microfluidic device that was connected to a bioreactor system and maintained under pulsatile flow (physiological-like flow-rate 10 ml/min) to induce mechanical stimulation of the tissue in culture (dynamic culturing). At day 14, hiPSCs-derived arterial ECs were seeded in the hiTEV lumen at the seeding density of 0.5×10^6 cells/cm^2 in a seeding volume of about 100 μl, and carefully rotated to allow for even seeding throughout the lumen surface. Henceforth, the hiTEVs were kept in static culture in a culturing medium prepared as follows: ½ iSMC- medium and ½ iECs medium for 7 days,and moved to dynamic conditioning within the microfluidic device at day 21 till day 28, when disease modeling begun.

8.2. Disease modeling in vitro. At day 28, the hiTEVs were perfused with syngeneic iMp form 2 weeks-old Mp-factories. The cultring medium was prepared as follows: ⅓ iSMC- medium, ⅓ iECs medium and ⅓ iMp medium. The medium was changed every 3 days and at each medium change 500'000 Mp/ml were added alongside with LDL, ApoB100 200 mg/dl (LeeBio) in a final volume of 50ml. The disease modeling time continued for 28 additional days (4 weeks). At the end of the disease modeling time, the iTEV could be easily harvested and further processed.

9. Computational fluid dynamic model

9.1 CAD modeling and mesh creation. A computer-aided design model (CAD) of the components of the fluidic device was generated using Autodesk Fusion 360. The Standard Tessellation Language file (STL) was exported into STAR-CCM+ for mesh rendering. Briefly, the model was imported into 3D CAD

and used to create a CAD imprint operation. The inner volume of the device was extracted via seed point and assigned to the region. To increase mesh resolution all boundaries were split into separate entities to make it easier to control the resolution of each separate group of surfaces. Hence, the obstacles were merged to allow targeted surface control on the mesh resolution.

9.2 Atheroscerosis modeling in silico. To model the behaviour of LDL within the device we used the Navier-Stokes equations and considered LDL as passive scalar with a diffusion coefficient determined by the Stokes-Einstein equations, which are aimed at modelling the diffusion of particles undergoing Brownian motion in a fluid at uniform temperature, and at relating the particle diameter to their diffusion and hence the Schmidt number (ratio of scalar diffusivity to viscous diffusion). All was discretized using unstructured finite-volume. LDL was considered as weakly negatively buoyant particle and, for modelling purposes, was provided at a inlet concentration of 190 mg/dl with a mass of 4.98159×10^{-21}kg and a density of 480.3029 kg/m^3. Hence, we performed a one-way coupling where only the flow influences particles and not vice versa. We instructed the code to sample impact and to register and remove the LDL particles when hitting a solid surface (e.g., inner vessel lumen), to not influence any subsequent impact. To estimate the accumulated particles within the vessels we measured the flux of the passive scalar. In detail, we multiplied the mass flow rate with time to obtain information on the magnitude of the mass flow (m= kg/m^2), and the putative surface growth rate. Knowing the density of the particles (ρ) we could then infer the measure of the surface growth ($\Delta x = m/ \rho$). Importantly, the growth rate depends linearly on the concentration at the inlet.

10. FnBPA5 peptide treatment

10.1. FnBPA5 preparation. The FnBPA5 peptides were commercially synthesized and HPLC-purified (Peptide Specialty Laboratories GmbH, Heidelberg, Germany, or Pichem GmbH, Graz, Austria). A spacer consisting of three glycines and a cysteine residue at the N-terminus of the original peptide sequence from *S. aureus* was introduced. The cysteine was introduced for further modifications with fluorescent dye (Cy5). Lyophilized peptides were dissolved in water (TraceSELECT® quality, Sigma) with 10% Dimethylformamide (DMF, Sigma) and stored at –20°C for further usage.

10.2. FnBPA5 staining of histological tissue sections and data analysis

For immunohistochemistry freshly dissected arteries were embedded in OTC matrix, frozen on dry-ice, and cut into 20 μm sections. Non-fixed cryo-sectioned tissue were thawed, rinsed with PBS to remove all the soluble components, blocked for 30 min with 5% BSA in PBS and incubated for 60 min with 5 µg/ml FnBPA5-Cy5. After one washing step the tissues were fixed in 4% PFA in PBS for 10 min. Samples were blocked in PBS with 5% BSA for 30 min and incubated with polyclonal rabbit anti-fibronectin antibody (Supplementary Table 5). The primary antibody solution was removed, and samples were washed before incubation with secondary goat anti-rabbit Alexa-546 (Supplementary Table 5) antibody solution for 45 min. After another washing step, samples were mounted using Prolong Antifade Gold with DAPI (Invitrogen). The image was acquired using an Olympus FV1000 confocal microscope equipped with a 10× air or 40× water objective. Whole tissue section was visualized by stitching together individual fields of view using the grid/collection stitching plugin in ImageJ. For image analysis at least 30 images per condition from 3 samples were analyzed for pixel-by-pixel signal intensity of Fn and FnBPA5 and graphed without further normalization. The microscope setting was kept the same during image acquisition for comparative analysis of signal intensity.

11. Satatistical analysis

Data were tested for normality and lognormality test. 4 different tests were performed: Anderson-Darling, D'Agostino and Pearson test, Shapiro-Wilk and Kolmogrov-Smirnov test. We then applied the Mixed-effects model with the Geisser-Greenhouse correction and post-hoc corrected for multiple comparison using the Dunnet Test. We accounted for the inter-donor (cell line) variability by increasing the false discovery rate to 0.1 (90% confidence interval). We show the *p* values for a FDR of 0.1.

Acknowledgments

AM was supported by a Start-up grant from the Center for Applied Biology and Molecular Medicine (CABMM) of the University of Zurich, and by a Spark grant from the Swiss National Science Foundation (SNSF, CRSK-3_190579/1). AM acknowledges Stephanie Davaz for the technical help in culturing and characterizing iECs and iSMCs, and Dr. Emanuela Fioretta for the insightful scientific exchanges. WH

was supported by a SNSF Sinergia grant (177195) and a pilot grant of the *Oxford – McGill –* Zurich Partnership in Neuroscience.

Author Contributions

AM conceptualized the experiments, designed the model and the microfluidic device components under BW and SPH supervision. AM differentiated and characterized hiPSCs and performed the tissue engineering experiments. CG and AM performed the flow cytometry experiments and analyzed the results. VH and VV provided the FnBPA5 peptide, VH, and AM stained, acquired, and analyzed the samples. KC and JHW developed the CFD model. WH and AM differentiated hiPSCs into iMp and maintained the iMp factories for the experiments. WH performed the LDL uptake assays. AVE, BW, AM, and SPH obtained fundings for the experiments. AM wrote the manuscript with the help of CG, WH, VH, and MYE. All the co-authors contributed to the final version of the manuscript.

Competing Interest statement

The authors declare no competing interests.

References

1 Libby, P. *et al.* Atherosclerosis. *Nat Rev Dis Primers* **5**, 56, doi:10.1038/s41572-019-0106-z (2019).
2 Yahagi, K. *et al.* Pathophysiology of native coronary, vein graft, and in-stent atherosclerosis. *Nat Rev Cardiol* **13**, 79-98, doi:10.1038/nrcardio.2015.164 (2016).
3 Kengne, A. P. & Echouffo-Tcheugui, J. B. Differential burden of peripheral artery disease. *Lancet Glob Health* **7**, e980-e981, doi:10.1016/s2214-109x(19)30293-1 (2019).
4 Bentzon, J. F., Otsuka, F., Virmani, R. & Falk, E. Mechanisms of plaque formation and rupture. *Circ Res* **114**, 1852-1866, doi:10.1161/circresaha.114.302721 (2014).
5 Wolf, D. & Ley, K. Immunity and Inflammation in Atherosclerosis. *Circ Res* **124**, 315-327, doi:10.1161/circresaha.118.313591 (2019).
6 Chait, A. & Bornfeldt, K. E. Diabetes and atherosclerosis: is there a role for hyperglycemia? *J Lipid Res* **50 Suppl**, S335-339, doi:10.1194/jlr.R800059-JLR200 (2009).
7 Libby, P. Inflammation in atherosclerosis. *Nature* **420**, 868-874, doi:10.1038/nature01323 (2002).
8 von Eckardstein, A., Nofer, J. R. & Assmann, G. High density lipoproteins and arteriosclerosis. Role of cholesterol efflux and reverse cholesterol transport. *Arterioscler Thromb Vasc Biol* **21**, 13-27, doi:10.1161/01.atv.21.1.13 (2001).
9 Hahn, C. & Schwartz, M. A. The role of cellular adaptation to mechanical forces in atherosclerosis. *Arterioscler Thromb Vasc Biol* **28**, 2101-2107, doi:10.1161/atvbaha.108.165951 (2008).
10 Simmons, R. D., Kumar, S. & Jo, H. The role of endothelial mechanosensitive genes in atherosclerosis and omics approaches. *Arch Biochem Biophys* **591**, 111-131, doi:10.1016/j.abb.2015.11.005 (2016).
11 Gimbrone, M. A., Jr. & Garcia-Cardena, G. Endothelial Cell Dysfunction and the Pathobiology of Atherosclerosis. *Circ Res* **118**, 620-636, doi:10.1161/circresaha.115.306301 (2016).
12 Goldberg, I. J. & Bornfeldt, K. E. Lipids and the endothelium: bidirectional interactions. *Curr Atheroscler Rep* **15**, 365, doi:10.1007/s11883-013-0365-1 (2013).
13 Kiener, P. A. *et al.* Immune complexes of LDL induce atherogenic responses in human monocytic cells. *Arterioscler Thromb Vasc Biol* **15**, 990-999, doi:10.1161/01.atv.15.7.990 (1995).
14 Frostegard, J., Huang, Y. H., Ronnelid, J. & Schafer-Elinder, L. Platelet-activating factor and oxidized LDL induce immune activation by a common mechanism. *Arterioscler Thromb Vasc Biol* **17**, 963-968, doi:10.1161/01.atv.17.5.963 (1997).
15 Deguchi, J. O. *et al.* Inflammation in atherosclerosis: visualizing matrix metalloproteinase action in macrophages in vivo. *Circulation* **114**, 55-62, doi:10.1161/CIRCULATIONAHA.106.619056 (2006).
16 Robert, J. *et al.* A three-dimensional engineered artery model for in vitro atherosclerosis research. *PLoS One* **8**, e79821, doi:10.1371/journal.pone.0079821 (2013).
17 Mallone, A., Stenger, C., Von Eckardstein, A., Hoerstrup, S. P. & Weber, B. Biofabricating atherosclerotic plaques: In vitro engineering of a three-dimensional human fibroatheroma model. *Biomaterials* **150**, 49-59, doi:10.1016/j.biomaterials.2017.09.034 (2018).
18 Chiu, J. J. & Chien, S. Effects of disturbed flow on vascular endothelium: pathophysiological basis and clinical perspectives. *Physiol Rev* **91**, 327-387, doi:10.1152/physrev.00047.2009 (2011).
19 Mundi, S. *et al.* Endothelial permeability, LDL deposition, and cardiovascular risk factors-a review. *Cardiovasc Res* **114**, 35-52, doi:10.1093/cvr/cvx226 (2018).
20 Head, T., Daunert, S. & Goldschmidt-Clermont, P. J. The Aging Risk and Atherosclerosis: A Fresh Look at Arterial Homeostasis. *Front Genet* **8**, 216, doi:10.3389/fgene.2017.00216 (2017).
21 Kirkton, R. D. *et al.* Bioengineered human acellular vessels recellularize and evolve into living blood vessels after human implantation. *Sci Transl Med* **11**, doi:10.1126/scitranslmed.aau6934 (2019).
22 Hoerstrup, S. P. *et al.* Tissue engineering of functional trileaflet heart valves from human marrow stromal cells. *Circulation* **106**, I143-150 (2002).
23 Emmert, M. Y. *et al.* Computational modeling guides tissue-engineered heart valve design for long-term in vivo performance in a translational sheep model. *Sci Transl Med* **10**, doi:10.1126/scitranslmed.aan4587 (2018).
24 Fioretta, E. S. *et al.* (J Am Coll Cardiol Basic Trans Science, 2019).
25 Driessen-Mol, A. *et al.* Transcatheter implantation of homologous "off-the-shelf" tissue-engineered heart valves with self-repair capacity: long-term functionality and rapid in vivo remodeling in sheep. *J Am Coll Cardiol* **63**, 1320-1329, doi:10.1016/j.jacc.2013.09.082 (2014).
26 Van Vre, E. A., Van Brussel, I., Bosmans, J. M., Vrints, C. J. & Bult, H. Dendritic cells in human atherosclerosis: from circulation to atherosclerotic plaques. *Mediators Inflamm* **2011**, 941396, doi:10.1155/2011/941396 (2011).
27 Ponticos, M. & Smith, B. D. Extracellular matrix synthesis in vascular disease: hypertension, and atherosclerosis. *J Biomed Res* **28**, 25-39, doi:10.7555/jbr.27.20130064 (2014).
28 Rekhter, M. D. Collagen synthesis in atherosclerosis: too much and not enough. *Cardiovasc Res* **41**, 376-384, doi:10.1016/s0008-6363(98)00321-6 (1999).
29 Cocciolone, A. J. *et al.* Elastin, arterial mechanics, and cardiovascular disease. *Am J Physiol Heart Circ Physiol* **315**, H189-h205, doi:10.1152/ajpheart.00087.2018 (2018).
30 Feaver, R. E., Gelfand, B. D., Wang, C., Schwartz, M. A. & Blackman, B. R. Atheroprone hemodynamics regulate fibronectin deposition to create positive feedback that sustains endothelial inflammation. *Circ Res* **106**, 1703-1711, doi:10.1161/circresaha.109.216283 (2010).
31 Duscher, D. *et al.* Mechanotransduction and fibrosis. *J Biomech* **47**, 1997-2005, doi:10.1016/j.jbiomech.2014.03.031 (2014).
32 Collins, C. *et al.* Haemodynamic and extracellular matrix cues regulate the mechanical phenotype and stiffness of aortic endothelial cells. *Nat Commun* **5**, 3984, doi:10.1038/ncomms4984 (2014).
33 Arnoldini, S. *et al.* Novel peptide probes to assess the tensional state of fibronectin fibers in cancer. *Nat Commun* **8**, 1793, doi:10.1038/s41467-017-01846-0 (2017).
34 Chang, W. G. & Niklason, L. E. A short discourse on vascular tissue engineering. *NPJ Regen Med* **2**, doi:10.1038/s41536-017-0011-6 (2017).
35 Doran, A. C., Meller, N. & McNamara, C. A. Role of smooth muscle cells in the initiation and early progression of atherosclerosis. *Arterioscler Thromb Vasc Biol* **28**, 812-819, doi:10.1161/atvbaha.107.159327 (2008).
36 Binder, C. J. *et al.* The year 2019 in Atherosclerosis. *Atherosclerosis* **299**, 67-75, doi:10.1016/j.atherosclerosis.2020.03.018 (2020).
37 Zhang, J. *et al.* Functional characterization of human pluripotent stem cell-derived arterial endothelial cells. *Proc Natl Acad Sci U S A* **114**, E6072-e6078, doi:10.1073/pnas.1702295114 (2017).
38 Yang, L. *et al.* Differentiation of Human Induced-Pluripotent Stem Cells into Smooth-Muscle Cells: Two Novel Protocols. *PLoS One* **11**, e0147155, doi:10.1371/journal.pone.0147155 (2016).
39 Generali, M. *et al.* Autologous endothelialized small-caliber vascular grafts engineered from blood-derived induced pluripotent stem cells. *Acta Biomater* **97**, 333-343, doi:10.1016/j.actbio.2019.07.032 (2019).
40 Caro, C. G., Fitz-Gerald, J. M. & Schroter, R. C. Arterial wall shear and distribution of early atheroma in man. *Nature* **223**, 1159-1160, doi:10.1038/2231159a0 (1969).

41 Malek, A. M., Alper, S. L. & Izumo, S. Hemodynamic shear stress and its role in atherosclerosis. *JAMA* **282**, 2035-2042, doi:10.1001/jama.282.21.2035 (1999).

42 van Wilgenburg, B., Browne, C., Vowles, J. & Cowley, S. A. Efficient, long term production of monocyte-derived macrophages from human pluripotent stem cells under partly-defined and fully-defined conditions. *PLoS One* **8**, e71098, doi:10.1371/journal.pone.0071098 (2013).

43 Haenseler, W. *et al.* A Highly Efficient Human Pluripotent Stem Cell Microglia Model Displays a Neuronal-Co-culture-Specific Expression Profile and Inflammatory Response. *Stem Cell Reports* **8**, 1727-1742, doi:10.1016/j.stemcr.2017.05.017 (2017).

44 Quintar, A. *et al.* Endothelial Protective Monocyte Patrolling in Large Arteries Intensified by Western Diet and Atherosclerosis. *Circ Res* **120**, 1789-1799, doi:10.1161/CIRCRESAHA.117.310739 (2017).

45 Buscher, K., Marcovecchio, P., Hedrick, C. C. & Ley, K. Patrolling Mechanics of Non-Classical Monocytes in Vascular Inflammation. *Front Cardiovasc Med* **4**, 80, doi:10.3389/fcvm.2017.00080 (2017).

46 Liu, B. & Tang, D. Computer simulations of atherosclerotic plaque growth in coronary arteries. *Mol Cell Biomech* **7**, 193-202 (2010).

47 Moore, K. J., Sheedy, F. J. & Fisher, E. A. Macrophages in atherosclerosis: a dynamic balance. *Nat Rev Immunol* **13**, 709-721, doi:10.1038/nri3520 (2013).

48 Randolph, G. J. Mechanisms that regulate macrophage burden in atherosclerosis. *Circ Res* **114**, 1757-1771, doi:10.1161/circresaha.114.301174 (2014).

49 Amir el, A. D. *et al.* viSNE enables visualization of high dimensional single-cell data and reveals phenotypic heterogeneity of leukemia. *Nat Biotechnol* **31**, 545-552, doi:10.1038/nbt.2594 (2013).

50 Fernandez, D. M. *et al.* Single-cell immune landscape of human atherosclerotic plaques. *Nat Med* **25**, 1576-1588, doi:10.1038/s41591-019-0590-4 (2019).

51 Koltsova, E. K. & Ley, K. How dendritic cells shape atherosclerosis. *Trends Immunol* **32**, 540-547, doi:10.1016/j.it.2011.07.001 (2011).

52 Soilleux, E. J., Morris, L. S., Trowsdale, J., Coleman, N. & Boyle, J. J. Human atherosclerotic plaques express DC-SIGN, a novel protein found on dendritic cells and macrophages. *J Pathol* **198**, 511-516, doi:10.1002/path.1205 (2002).

53 Gawaz, M., Stellos, K. & Langer, H. F. Platelets modulate atherogenesis and progression of atherosclerotic plaques via interaction with progenitor and dendritic cells. *J Thromb Haemost* **6**, 235-242, doi:10.1111/j.1538-7836.2007.02867.x (2008).

54 Di Gregoli, K. *et al.* MicroRNA-181b Controls Atherosclerosis and Aneurysms Through Regulation of TIMP-3 and Elastin. *Circ Res* **120**, 49-65, doi:10.1161/CIRCRESAHA.116.309321 (2017).

55 Maurice, P. *et al.* Elastin fragmentation and atherosclerosis progression: the elastokine concept. *Trends Cardiovasc Med* **23**, 211-221, doi:10.1016/j.tcm.2012.12.004 (2013).

56 M., F. C. *et al.* (Matrix Biology Plus, 2020).

57 Fan, J. *et al.* Rabbit models for the study of human atherosclerosis: from pathophysiological mechanisms to translational medicine. *Pharmacol Ther* **146**, 104-119, doi:10.1016/j.pharmthera.2014.09.009 (2015).

58 Getz, G. S. & Reardon, C. A. Use of Mouse Models in Atherosclerosis Research. *Methods Mol Biol* **1339**, 1-16, doi:10.1007/978-1-4939-2929-0_1 (2015).

59 Lichtman, A. H. Adaptive immunity and atherosclerosis: mouse tales in the AJP. *Am J Pathol* **182**, 5-9, doi:10.1016/j.ajpath.2012.10.006 (2013).

60 Macritchie, N. *et al.* Plasmacytoid dendritic cells play a key role in promoting atherosclerosis in apolipoprotein E-deficient mice. *Arterioscler Thromb Vasc Biol* **32**, 2569-2579, doi:10.1161/atvbaha.112.251314 (2012).

61 Shim, J., Al-Mashhadi, R. H., Sorensen, C. B. & Bentzon, J. F. Large animal models of atherosclerosis--new tools for persistent problems in cardiovascular medicine. *J Pathol* **238**, 257-266, doi:10.1002/path.4646 (2016).

62 Davis, B. T. *et al.* Targeted disruption of LDLR causes hypercholesterolemia and atherosclerosis in Yucatan miniature pigs. *PLoS One* **9**, e93457, doi:10.1371/journal.pone.0093457 (2014).

63 Blaton, V. & Peeters, H. The nonhuman primates as models for studying human atherosclerosis: studies on the chimpanzee, the baboon and the rhesus macacus. *Adv Exp Med Biol* **67**, 33-64 (1976).

64 Escate, R., Padro, T. & Badimon, L. LDL accelerates monocyte to macrophage differentiation: Effects on adhesion and anoikis. *Atherosclerosis* **246**, 177-186, doi:10.1016/j.atherosclerosis.2016.01.002 (2016).

65 Bjorkerud, B. & Bjorkerud, S. Contrary effects of lightly and strongly oxidized LDL with potent promotion of growth versus apoptosis on arterial smooth muscle cells, macrophages, and fibroblasts. *Arterioscler Thromb Vasc Biol* **16**, 416-424 (1996).

66 Kwak, B. R. *et al.* Biomechanical factors in atherosclerosis: mechanisms and clinical implications. *Eur Heart J* **35**, 3013-3020, 3020a-3020d, doi:10.1093/eurheartj/ehu353 (2014).

67 Cybulsky, M. I., Cheong, C. & Robbins, C. S. Macrophages and Dendritic Cells: Partners in Atherogenesis. *Circ Res* **118**, 637-652, doi:10.1161/circresaha.115.306542 (2016).

68 Weber, B. & Hoerstrup, S. P. Human bioengineered artery models for in vitro atherosclerosis research: fact or fiction? *Altern Lab Anim* **42**, P28-32 (2014).

69 Viola, V. & Caleb, W. (DMM, 2020).

70 Milei, J. *et al.* Perinatal and infant early atherosclerotic coronary lesions. *Can J Cardiol* **24**, 137-141, doi:10.1016/s0828-282x(08)70570-1 (2008).

71 Hong, Y. M. Atherosclerotic cardiovascular disease beginning in childhood. *Korean Circ J* **40**, 1-9, doi:10.4070/kcj.2010.40.1.1 (2010).

72 Johnson, A. M. *et al.* Military combat and burden of subclinical atherosclerosis in middle aged men: the ARIC study. *Prev Med* **50**, 277-281, doi:10.1016/j.ypmed.2010.02.009 (2010).

73 Hansen, T., Wikström, J., Johansson, L. O., Lind, L. & Ahlström, H. The prevalence and quantification of atherosclerosis in an elderly population assessed by whole-body magnetic resonance angiography. *Arterioscler Thromb Vasc Biol* **27**, 649-654, doi:10.1161/01.ATV.0000255310.47940.3b (2007).

74 Ammirati, E., Moroni, F., Magnoni, M. & Camici, P. G. The role of T and B cells in human atherosclerosis and atherothrombosis. *Clin Exp Immunol* **179**, 173-187, doi:10.1111/cei.12477 (2015).

75 Williams, K. J. & Tabas, I. The response-to-retention hypothesis of early atherogenesis. *Arterioscler Thromb Vasc Biol* **15**, 551-561, doi:10.1161/01.atv.15.5.551 (1995).

76 Ikuno, T. *et al.* Efficient and robust differentiation of endothelial cells from human induced pluripotent stem cells via lineage control with VEGF and cyclic AMP. *PLoS One* **12**, e0173271, doi:10.1371/journal.pone.0173271 (2017).

77 Fernandes, H. J. *et al.* ER Stress and Autophagic Perturbations Lead to Elevated Extracellular alpha-Synuclein in GBA-N370S Parkinson's iPSC-Derived Dopamine Neurons. *Stem Cell Reports* **6**, 342-356, doi:10.1016/j.stemcr.2016.01.013 (2016).

78 Haenseler, W. *et al.* Excess alpha-synuclein compromises phagocytosis in iPSC-derived macrophages. *Sci Rep* **7**, 9003, doi:10.1038/s41598-017-09362-3 (2017).